

OPEN ACCESS

EDITED BY

Jorge Luis Chau,
Leibniz Institute of Atmospheric Physics
(LG), Germany

REVIEWED BY

Savely M. Grach,
Lobachevsky State University of Nizhny
Novgorod, Russia
Federico Gasperini,
Orion Space Solutions LLC, United States

*CORRESPONDENCE

Petra Koucká Knížová,
✉ pkn@ufa.cas.cz

RECEIVED 30 March 2023

ACCEPTED 05 June 2023

PUBLISHED 23 June 2023

CITATION

Koucká Knížová P, Potužníková K,
Podolská K, Hannawald P, Mošna Z,
Kouba D, Chum J, Wüst S, Bittner M and
Kerum J (2023), Multi-instrumental
observation of mesoscale tropospheric
systems in July 2021 with a potential
impact on ionospheric variability in
midlatitudes.
Front. Astron. Space Sci. 10:1197157.
doi: 10.3389/fspas.2023.1197157

COPYRIGHT

© 2023 Koucká Knížová, Potužníková,
Podolská, Hannawald, Mošna, Kouba,
Chum, Wüst, Bittner and Kerum. This is
an open-access article distributed under
the terms of the [Creative Commons
Attribution License \(CC BY\)](https://creativecommons.org/licenses/by/4.0/). The use,
distribution or reproduction in other
forums is permitted, provided the
original author(s) and the copyright
owner(s) are credited and that the
original publication in this journal is
cited, in accordance with accepted
academic practice. No use, distribution
or reproduction is permitted which does
not comply with these terms.

Multi-instrumental observation of mesoscale tropospheric systems in July 2021 with a potential impact on ionospheric variability in midlatitudes

Petra Koucká Knížová ^{1*}, Kateřina Potužníková²,
Kateřina Podolská ¹, Patrick Hannawald³, Zbyšek Mošna¹,
Daniel Kouba¹, Jaroslav Chum¹, Sabine Wüst ³,
Michael Bittner³ and Jacek Kerum²

¹Department of Ionosphere and Aeronomy, Institute of Atmospheric Physics, Czech Academy of Sciences, Prague, Czechia, ²Department of Meteorology, Institute of Atmospheric Physics, Czech Academy of Sciences, Prague, Czechia, ³German Aerospace Center, German Remote Sensing Data Center, Weßling, Germany

The ionosphere as a part of Earth's atmosphere supports a wide range of oscillations, of which acoustic-gravity waves (AGWs) form an important part. AGWs distribute energy and momentum from the source region over large distances. A significant portion of AGWs originates in the lower atmosphere and propagates through the atmosphere up to the ionospheric heights where, due to the coupling between neutral and ionized particles, it could be detected as wavelike disturbances of the plasma. Primarily, the ionospheric behavior is driven by solar and geomagnetic activity, while the influence from neutral and below-laying regions of the atmosphere most of the time forms a substantially smaller part of the observed variability. However, it could significantly alter ionospheric behavior. Our study is limited to a time span of rather low solar and geomagnetic activity in order to highlight neutral atmosphere influence. In this study, we focus on two tropospheric situations above Europe that may lead to AGW generation, which propagate up to the F-layer where they potentially induce variability that we observe within ionospheric plasma parameters.

KEYWORDS

gravity wave activity, short-term variability, troposphere, cyclone, atmospheric coupling, mesosphere, ionosphere

1 Introduction

The ionosphere is a part of the atmosphere that significantly influences the propagation of electromagnetic signals due to the presence of ionized particles (recently, for instance, in [Radicella and Migoya-Orué, 2021](#)). The state of the ionosphere is predominantly driven by the (quasi) periodic as well as irregular solar activity (e.g., [Borries et al., 2015](#); [Bederman et al., 2018](#)) and geomagnetic activity (e.g., [Pröhl, 1995](#); [Buonsanto, 1999](#), among others). The importance of a neutral atmosphere influence on the ionosphere as high as the F2 layer ionosphere was pointed out in the 1970s. Increasing interest of the ionosphere scientific community in this topic is well observed in the last two decades of the 20th century.

In past years, it has been widely accepted that the ionosphere is affected by pronounced phenomena originating within the neutral atmosphere as close as to the Earth's surface in the troposphere and stratosphere, i.e., in the regions located below the mesosphere and lower thermosphere (MLT) region (see for instance Laštovička, 2006; Kazimirovski and Kokourov, 1991; Koucká Knížová et al., 2021). Medvedev and Gavrilov (1995) numerically simulated the tropospheric meso- and macro-scale source evolution and consequent propagation up to the thermospheric heights. Most of the wave energy propagates quasi-horizontally, and part of the energy is transported into the upper atmosphere by internal gravity waves, which can create regions of wave disturbances in the mesosphere/lower thermosphere. Their study also involved real meteorological geopotential data. They identified the following effective meteorological sources: a center of cyclones, a center of anticyclones, a curvature of jet streams, a saddle point between a cyclone and an anticyclone, and an outlying area of vortices.

A large statistical study was performed by Forbes et al. (2000) who analyzed the impact of “meteorological influences” defined as non-periodic dynamical effects originating in the lower atmosphere on the F2 region using data from more than 100 ionosondes during the period 1967–1989. They showed that the ionospheric variability of meteorological origin is approximately $\pm 25\%$ – 35% at periods of a few hours to 1–2 days and approximately $\pm 15\%$ – 20% at periods of approximately 2–30 days compared to the mean of ionospheric variability, at all latitudes. However, Rishbeth and Mendillo (2001) suggested that the contribution of solar/geomagnetic activity and lower-atmosphere forcing to day-to-day ionosphere variability should be equally considered. Pedatella and Liu (2018) demonstrated that omitting lower-atmosphere variability leads to uncertainty in the ionosphere response to a geomagnetic storm that is typically $\sim 20\%$ – 40% but can be as large as 100% regionally.

As mentioned previously, the ionosphere represents the transition zone from the space environment (plasma) to the neutral atmosphere being coupled both from above into the fully ionized Earth's magnetosphere and from below into the neutral atmosphere. The behavior of the environment above and below significantly differs being determined by electromagnetic forcing and collisions, respectively. Ionospheric plasma is only a weakly ionized medium. With increasing height, the neutral particle concentration decreases, while due to ionization processes, the concentration of charged particles increases, reaching its maximum within the F2 layer, where the maximum electron concentration is usually located. The ionization degree here reaches values of up to approximately 0.01, and the charged particles are directly influenced by the neutral particles. With increasing height, collisions are less important and plasma motion is more determined by the electromagnetic forcing. Neutral and charged particles are strongly coupled. Their interactions lead to mass, momentum, and energy transfers.

On longer time scales, the effects of large circulation structures within variability of ionospheric parameters were reported. In particular, Chang et al. (2018) reported the dependence of the S4 scintillation index in the E-region midlatitudes on variation of the El Niño–Southern Oscillation (ENSO) in the troposphere. ENSO signatures can be transmitted to Es formation mechanisms, potentially through the modulation of vertically propagating

atmospheric tides that alter lower thermospheric wind shears. A substantial response within the ionospheric plasma parameters was identified during sudden stratospheric warmings (SSWs) (see for instance Mošna et al., 2021; Korenkov et al., 2012; Siddiqui et al., 2021). In the coupling during SSWs, planetary-scale waves, particularly semi-diurnal solar and lunar tides, play a key role in altering atmospheric circulation (Pancheva et al., 2008; Pedatella and Forbes, 2010).

It has been shown that severe tropospheric events such as cyclones (Guha et al., 2016; Koucká Knížová et al., 2020; Zakharov and Sigachev, 2022), hurricanes (Bauer, 1958; Li et al., 2017), typhoons (Xiao et al., 2007; Chum et al., 2018), thunderstorms (Blanc et al., 2014; Lay, 2018; Rahmani et al., 2020), synoptic-scale frontal systems (Boška and Šauli, 2001; Šauli and Boška, 2001), storms (Borchevskina et al., 2020; Borchevskina et al., 2020), and tornadoes (Hung et al., 1979) influence the ionosphere. Acoustic-gravity waves (AGWs) and their propagation to the ionosphere play an important role in vertical coupling (Kazimirovsky and Kokourov, 1991; Bishop et al., 2006 and references therein) as the amplitudes of AGWs increase significantly in the thermosphere and the waves dissipate in the thermospheric viscous fluid (Vadas et al., 2015), resulting in a change in the momentum (acceleration) and internal energy of the substantial part of the ionosphere.

The stratosphere also affects the state of the ionosphere. An increasing number of reports indicate that SSWs affect the mesosphere–thermosphere–ionosphere region mainly in the equatorial and low latitudes (Chau et al., 2012; Yiğit and Medvedev, 2015) but, as recently demonstrated, also in middle latitudes (Goncharenko and Zhang, 2008; Goncharenko et al., 2018; Siddiqui et al., 2021).

Within a previous study, 13 years of routine radiosonde data from Prague (50.008°N, 14.448°E) with temporal highly resolved temperature, pressure, and wind measurements were analyzed with respect to gravity wave activity in the lower stratosphere (Kramer et al., 2016). The data indicated that the maxima of gravity wave activity and vertical flux of horizontal momentum often appear together with minima in surface pressure. Kramer et al., 2015 reported about gravity waves which were excited above Mallorca (39.647°N, 2.689°E) during the passage of a cold front and which obviously managed—at least partly—to propagate up to the mesopause region.

Figure 1 shows one of our early detection/identification of AGW signatures on ionogram records using the now replaced ionosonde IPS 42 KEL Aerospace. It operated in the Průhonice Observatory till the beginning of 2004. An irregularity is well observed on the course of virtual reflection height at a fixed frequency as derived from raw ionograms. On the course of radiowave virtual reflection height, there occurred strong spread-F echo on 12 October. The echo registered at fixed frequency = 3 MHz arrived from a virtual height range of approximately 250 km–500 km, and the spread situation took place for a short period between 09 and 10 UTC.

Ionosondes and/or Digisondes regularly transmit electromagnetic waves vertically upward and register reflected waves. From the wave time of flight, they calculate the virtual height of the plasma with a concentration corresponding to the sounding frequency. The virtual height corresponds to a simplified

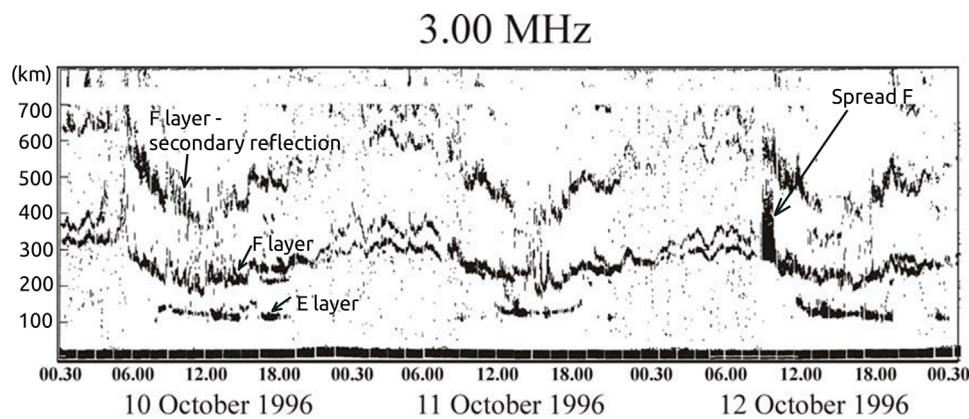


FIGURE 1

Observation of the passage of a cold front system on 12 October 1996 by Ionosonde IPS 42 KEL Aerospace in the Průhonice Observatory. This visualization shows the virtual height of vertical echo reflection at a fixed frequency of 3 MHz. The instrument did not distinguish between ordinary and extraordinary waves. A strong spread in the F-region is clearly seen as reflection in the interval 250 km–500 km visible on 12 October between 09 and 10 a.m. The geomagnetic activity was low to moderate.

situation in which an electromagnetic wave travels through vacuum up to the reflection point. This value is slightly higher than the true height because the signal's speed propagating in plasma is lower than the speed of light in the vacuum. The graph showing the dependence of the virtual height on the sounding frequency is called an ionogram, and it represents the standard output of the ionosondes and digisondes. The $h(f)$ characteristics depend on particular ionospheric conditions. In an ideal situation, the reflection occurs on the perfect plane. In a real situation, the reflection surface is usually undulated. It leads to the presence of a significant amount of off-vertical echoes. On the ionograms, one can observe deviations from ideal planar and stationary situations such as the spread of the echo signal, cusp stratification, and split double echo. The classification of ionogram scaling and interpretation can be found, for instance, in the manual of ionogram scaling (Wakai et al., 1987) or the URSI manual (UAG-23A, 1978). Off-vertical echo ionograms must be manually checked (Kouba and Koucká Knížová, 2011).

A particular type of the radiowave reflection represents the spread-F echo in range (height), frequency, or mixed form on ionograms. In such cases, the receiver registers several reflections from a range of heights and frequencies rather than one vertical reflection. It means that the reflection plane of constant concentration is not an ideal plane but rather undulated and/or contains density irregularities. Spread-F-type reflection ionograms are often recorded during episodes of high geomagnetic activity in association with traveling ionospheric disturbances (TIDs). Bowman et al. (1987) proposed that a deformed ionosphere by the passage of TIDs was the main factor for spread F during daytime ionograms at midlatitudes; Jiang et al. (2016) reported the presence of TIDs before the occurrence of daytime spread F and suggested that downward vertical neutral winds excited by traveling atmospheric disturbances/atmospheric gravity waves might play a significant role in forming daytime spread F during geomagnetic storms; Jonah et al. (2018) reported the presence of both equatorward propagating large-scale TIDs connected with enhanced auroral activity owing to geomagnetic storm

conditions and poleward propagating medium-scale TIDs likely induced by local atmospheric gravity wave sources originating from convection activities in the lower atmosphere during geomagnetic storm events in May 2017; Xiao et al. (2012) observed daytime ionospheric irregularities by HF Doppler sounding and suggested that a typhoon was a source of daytime spread F at midlatitude; Koucká Knížová et al. (2020) reported a spread-F echo situation associated with frontal cyclones of sub-synoptic scales that were very quickly moving over Central Europe. Further observations of spread-F ionograms in association with AGWs were also reported (Bowman, 1981; 1988; 1990; Dyson et al., 1995; Bencze and Bakki, 2002; Xiao et al., 2009; Pezzopane et al., 2011; Yu et al., 2016).

Usually, large-scale TIDs (LSTIDs) observed during episodes of increased geomagnetic activity and medium-scale TIDs (MSTIDs) were reported in connection with vertical coupling within the atmosphere. Upward propagation of AGWs depends on the state of the entire atmosphere from the troposphere up to the ionosphere. Fritts and Vadas (2008) identified three key influence parameters on GW survival and penetration to high altitudes. These major factors are refraction accompanying Doppler shifting by strong mean winds in the MLT and thermosphere, GW evanescence and reflection at turning levels, and viscous dissipation. The model study indicates changes in GW ability to reach high altitudes depending on solar forcing.

Wavelike structures in the midlatitude nightglow have been previously studied before satellite imagery. Taylor and Hapgood (1988) observed concentric gravity waves for a period of 10–20 min in the mesospheric nightglow (horizontal wavelength of the airglow structures was 26 km). They identified an isolated midlatitude summer thunderstorm (with a horizontal radius of 10 km) over the European continent as a possible source. A theoretical explanation for the source of oscillations in the form of penetrating convection in the growth phase of storms was proposed by Pierce and Coroniti (1966). Recently, the source of waves in the upper troposphere and stratosphere can be easily traced from satellite images (Yue et al., 2014).

Many past and recent satellite and radar measurements in the midlatitude region have focused on the interaction of gravity waves generated by different sources in the troposphere and their propagation upward into the ionosphere. Pavelin and Whiteway (2002) presented the case of radar observations of turbulence in the tropopause region generated by the interaction between an inertial gravity wave over the jet stream and a smaller-scale mountain wave. Bertin et al. (1978), based on geosatellite measurements, discussed the origin of a medium-scale gravity wave (for a period of less than 45 min) that was probably produced by the interaction of wind shear in the jet stream region and penetrative convective systems. Fritts and Alexander (2003) summarized the results of theoretical, numerical, and observational studies dealing with the sources and characteristics of gravity waves in the middle atmosphere (at altitudes between 10 and 100 km). This concludes that there is a need to extend both numerical studies and more detailed observations to quantify wave discontinuities caused by different sources, propagation conditions, etc., as discontinuities have a major impact on wave effects at higher altitudes, including instability processes, wave-wave interactions and mean flow, and secondary wave emission.

2 Motivation

Our study aimed to show tropospheric situations that may lead to observable Earth's atmosphere variability up to the heights of the F2 layer ionosphere. In this study, we focus on rather recent tropospheric cases. Due to coincidental occurrences of disturbances within mesosphere and ionosphere datasets, without solar-geomagnetic energetic impulses, we assume that we observe variability induced by AGWs launched by tropospheric systems.

We chose two particular synoptic situations that fall into periods of stable solar conditions and rather low (low-to-moderate) geomagnetic activity. The low geomagnetic activity was chosen in

order to highlight the effects of meteorological influence as much as possible as it is practically unfeasible to untangle and isolate the effects. During our time of interest, the geomagnetic activity is rather low ($Kp_{\text{mean}} = 1.26$ and $Kp_{\text{median}} = 1$; maximum value $Kp = 4+$ only once during the analyzed period). Solar activity characterized by solar flux F10.7 is stable with values $F10.7_{\text{mean}} = 81.06$ and $F10.7_{\text{median}} = 77.65$. Selected tropospheric situations differ in their nature. The first case of 13/14 July 2021 represents disturbances caused by convective upward motions in the squall line ahead of a cold front with heavy rainfall (Bernd cyclone). The second case occurred on 29 July 2021, and it was a polar front jet stream in the upper troposphere enhanced by orography with an atypical location of the jet stream.

Figure 2 shows the geomagnetic situation from 1 July to 15 August 2021 according to the finalized Kp-index and Ap-index (data from GFZ German Research Centre for Geosciences). Geomagnetic activity was low to moderate during all the studied periods. The activity shortly increases twice, reaching the values 4+ and 4-. On 14 July, for a few hours after 16 UT, the Kp index exceeded value 3. On 28 July, only two recorded Kp values reached 4-. The rest of the time recorded values remain below value 3. Therefore, we consider the analyzed time as rather geomagnetically quiet.

Our experimental datasets involved in this study cover the troposphere, mesosphere, and ionosphere. Tropospheric data consist of standard surface and radiosonde meteorological measurements, together with weather radar, as well as surface and upper-air weather maps. The datasets are completed by upper mesospheric/lower thermospheric airglow measurements taken by the FAIM2 (Fast Airglow IMager2) instrument operated by the German Aerospace Center at the Panská Ves Observatory (50.527°N, 14.568°E). Ionosphere datasets consist of vertical sounding data from Digisonde DPS-4D operating in the Průhonice Observatory, together with oblique sounding at fixed frequency continuous Doppler sounding (CDS) with the receiver located in Prague.

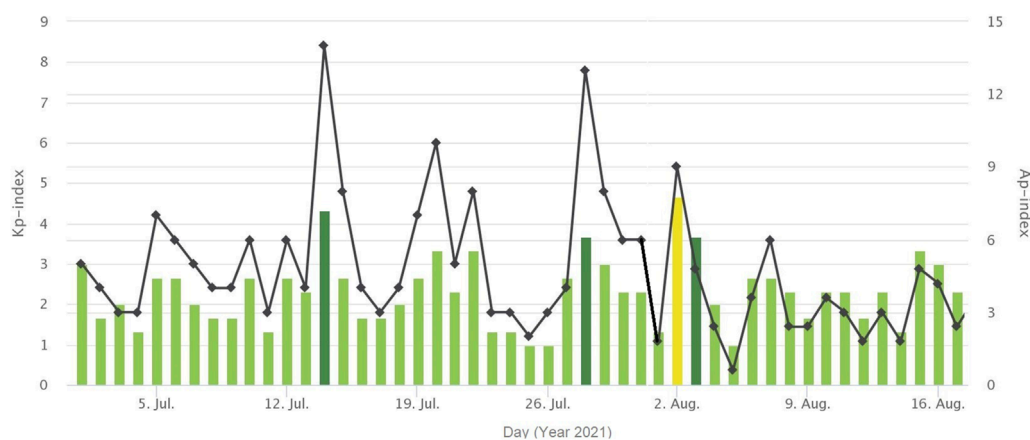


FIGURE 2

Geomagnetic situation from 1 July–15 August 2021. Geomagnetic activity is low to moderate during all the studied periods. The activity shortly increases twice reaching the values 4- and 4+. On 14 July, Kp increased for a few hours after 16:00 UTC exceeding value 3. On 28 July, only two recorded Kp values reached 4-. The rest of the time, the recorded values remain below value 3 according to the finalized Kp-index of GFZ Potsdam. The black line and points mark the daily value of the Ap-index (data from the GFZ German Research Centre for Geosciences).

3 Data

3.1 Tropospheric data

Meteorological datasets include standard weather measurements of temperature, pressure, and wind operated by the Institute of Atmospheric Physics, Czech Academy of Sciences (geographic coordinates 50.041°N, 14.477°E). For the description of the troposphere situation and development, we use surface pressure maps provided by WetterKontor at <https://www.wetterkontor.de/de/wetterlage.asp>, last access: 24 January 2023, and archived weather charts offered at <http://wetter3.de> and <https://www.firenzemeteo.it/>, last access: 24 January 2023, produced from data based on the US Global Forecast System (GFS) model and the model of the German Weather Service ICON. We also use the atmospheric vertical sounding radiometer data available at <https://weather.uwyo.edu/upperair/sounding.html>.

3.2 Mesospheric data

In particular, OH nightglow with a mean emission altitude of approximately 86 km is well-suited to investigate the dynamics in the upper mesosphere and lower thermosphere region (see [Wüst et al., 2023](#) and references given therein). The OH nightglow layer has its strongest emission in the short-wave infrared range at approximately 1.5–1.6 μm [rotational–vibrational transitions OH(3-1) and OH(4-2)]. Such ground-based observations of the OH nightglow layer are affected by clouds, and the best results are achieved at cloud-free nights. For the thermal convection event, clear-sky imager data are analyzed during the nights of 12–13 (5 h of good data quality), 14–15 (1.9 h of good data quality), and 15–16 (6.2 h of good data quality) July. No data are available for the nights of 13–14. For the event on 29 July, we analyzed the data of the nights of 28–29 (4.5 h of good data quality), 29–30 (5.4 h of good data quality), and 30–31 (2 h of good data quality) July.

The short-wave infrared camera FAIM2 observes the nightglow emission in the spectral range from 0.9 to 1.65 μm , taking one image every second during each night from sunset to sunrise. Due to the comparatively intense OH emissions, OH(3-1) and OH(4-2) are mainly observed using the camera; the strong O₂ emission at 1.26 μm decays relatively faster and is then weaker than the OH emission about 30 min after sunset ([Hannawald et al., 2016](#)). As previously mentioned, the camera is located at the observatory Panská Ves with the field of view (FOV) oriented to the south between the observatory and Prague. It has a size of approximately 27° times 33°, which corresponds to an area of approximately 47 km times 56 km at an altitude of 86 km and a spatial resolution of 180 m. The images are analyzed using a 2D-FFT in order to derive spatiotemporal wave parameters ([Hannawald et al., 2019](#)). However, the analyzed wave structures are, of course, limited to the FOV size (i.e., a maximum horizontal wavelength of approximately 47 km).

The images are analyzed using a 2D-FFT in order to derive spatiotemporal wave parameters. While the 2D-FFT analysis provides information about the horizontal wave parameters like horizontal wavelength and horizontal angle of propagation (with a 180° ambiguity), the temporal wave parameters are derived by

investigating these horizontal wave parameters for consecutive images. A wave event is defined as the occurrence of the same horizontal wavelength and angle of propagation (denoted as a “wave signature”) connected in time. Connected in time means that the wave signature is present in consecutive images (small time gaps are allowed). For each group of wave signatures connected in time, the change in the phase information (calculated by the 2D-FFT) with time is investigated to derive, e.g., the unambiguous direction of propagation and the phase speed (see [Hannawald et al., 2019](#) for a more detailed description of the analysis).

3.3 Ionospheric data

Continuous Doppler sounding is an effective continuous method for monitoring the state of the ionosphere ([Kouba and Chum, 2018](#)). It can detect ionospheric fluctuations of periods ~10 s and longer. The system is most suitable for studying waves of periods from ~20 s to ~100 min. The electromagnetic wave of fixed frequency is reflected from the ionosphere and detected in the receiver. In our study, we use a system that comprises three transmitters and one receiver. CDS measurement does not allow the determination of reflection height of the sounding signal. It is further determined from a nearby ionosonde. The best Doppler shift results are usually obtained when the reflection is obtained from the F2 layer (~180–300 km). If the reflection is from altitudes lower than ~150 km (E-layer), the Doppler shift is usually very small and often difficult to analyze. In addition, during summer days, if the D-layer is well-developed, the sounding radio signal might experience a strong attenuation (very weak signal is received) around noon. The specific frequencies of the individual transmitters are shifted by 4 Hz so that the signals of all transmitters could be displayed in one common Doppler shift spectrogram. Signals from the transmitter located in Panská Ves (50.528°N, 14.567°E) and received in Prague (50.041°N, 14.477°E) are used in this study. Further technical details can be found at https://www.ufa.cas.cz/DATA/files/oia/Doppler_des_365.pdf and in works by [Chum and Podolská \(2018\)](#), [Chum et al. \(2021\)](#), and [Laštovička and Chum \(2017\)](#). The system works for larger periods as well, but the ionosonde might be more advantageous since it provides information from the whole range of altitudes.

Digisonde for vertical ionospheric sounding operates on a similar principle. It transmits electromagnetic signals usually in a frequency range of 1–20 MHz and measures the time of flight of the reflected signal. In a regular sounding regime, it works typically with 15 min of repetition time. After the ionogram measurement, the system automatically searches for critical frequency and performs a restricted range drift measurement below the F2 layer critical frequency. Our Digisonde has a double-crossed delta transmitting antenna and four cross-loop receiving antennas. The configuration of the antenna field, together with coded signal and high number of transmitting signal repetitions, allows to identify parameters of the reflected wave. Afterward, the ionograms and drift data are manually checked and scaled for further processing ([Kouba and Koucká Knížová, 2011](#); [Kouba and Koucká Knížová, 2012](#); [Kouba and Koucká Knížová, 2016](#)). Ionograms and drift measurements are automatically sent into the world database GIRO (<https://giro.uml.edu/>). Digisonde data used in this study are measured

at the Průhonice Observatory (geographic coordinates 49.990°N, 14.539°E).

4 Observation

4.1 Tropospheric observation

First of all, it is important to mention that determining events such as atmospheric front transitions and convective storm development requires a great deal of experience and largely manual analysis of meteorological conditions both at synoptic and sub-synoptic scales. Not only does the stability of the air mass but also the overall dynamics of the troposphere play a role in determining the development of storms. An essential condition for the formation of severe convection is sufficient moisture in the lower levels of the troposphere and the upper-level divergent air flux (Kašpar et al., 2009). Surface measurements of meteorological conditions before and after the passage of the front are used to determine the passage of atmospheric fronts, especially significant changes in temperature and pressure tendencies, wind shifts, atmospheric precipitation, and

wind gusts. Another criterion is the strong horizontal temperature gradient at the 850 hPa geopotential level. In our analyses, we use the pseudo-equivalent potential temperature field, which synthetically represents both temperature and humidity characteristics at the lower part of the troposphere. Narrow transformation zones with a strong gradient of pseudo-equivalent potential temperature at 850 hPa locate the positions of fronts on the surface pressure field (Kašpar, 2003). Another criterion for assessing the dynamics of the troposphere is the density and curvature of isohypse of 500 hPa geopotential height. The 500-hPa maps show the main flow regime of the troposphere. In synoptic meteorology, a 500-hPa map is used to determine the speed and direction of synoptic patterns and thus middle latitude atmospheric dynamics at an altitude of approximately 5.5 km. The small distance between isobars at 500 hPa represents an area of strong pressure gradient and strong wind speed. We also use a pressure level of 300 hPa or usually 200 hPa in summer, located near the tropopause at an altitude of approximately 9 or 12 km, to assess tropospheric flow dynamics. This level is used to determine the location and character of the polar front (zonal/meridional) and the associated jet stream. The jet stream can, under certain conditions, intensify severe

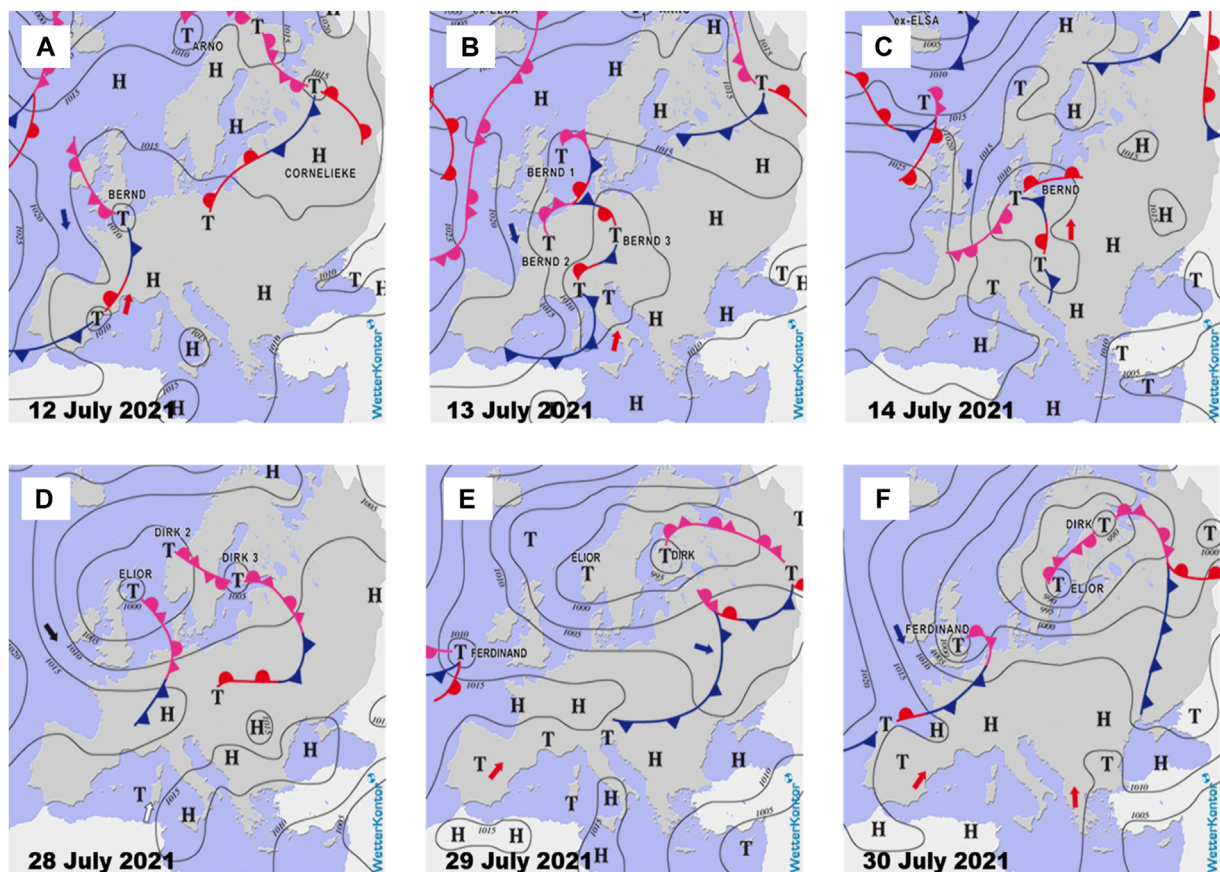


FIGURE 3

Surface pressure maps provided by WetterKontor, from <https://www.wetterkontor.de/wetterlage.asp>. Surface pressure is plotted with solid lines with 5-hPa steps. Atmospheric fronts (red curved lines with red semicircles that point in the direction of the warm front, blue curved lines with blue triangles that point in the direction of the cold front, and purple lines with alternating triangles and semicircles pointing in the direction in which the occluded front moves) and the locations of the centers of high- (H) and low- (T)-pressure systems are also presented. Upper panels (A–C) show the evolution of Cyclone Bernd, and bottom panels (D–F) show an atypical jet stream situation.

weather associated with a cold front. However, even a strong jet stream alone, without the accompanying effects of thunderstorms or sustained precipitation, can cause gravity waves to propagate into the ionosphere.

In this paper, we show two cases—a thermal convective event on 13 and 14 July 2021, associated with thunderstorms and convective precipitation occurring along boundaries of weather cold fronts, and an orographically driven convective event on 29 July 2021 in the jet stream region.

4.1.1 Thermal convection event of 13–14 July 2021 (Bernd cyclone)

The synoptic analysis given in Figures 3A–C shows that a relatively cold air mass from the Atlantic Ocean spreads over Western Europe. During this period, most of Eastern and Central Europe and the Mediterranean were affected by the southwesterly flow regime. (In meteorology, the direction given for the wind flow refers to the direction from which it comes.) Consequently, cold fronts formed at the surface over Central Europe on 12 July 2021. During the next 24 h, Central Europe was still under the influence of surface to upper-tropospheric flow of warm air originating from the Africa continent, supplemented by moisture from the Mediterranean. (The origin of the air mass mixed with dust from the Sahara is also evidenced by numerous observations of the yellowish color of the sky and clouds over the Czech Republic on 12 and 13 July.) The persistent advection of thermally unstable tropical

air mass caused both the waving of atmospheric fronts associated with cyclones and the regeneration of cyclones over Central Europe. Subsequently, organized thunderstorms (squall lines) occurred in warm sectors ahead of cold fronts. On 13 July, thunderstorms were recorded in Germany and also in the Czech Republic, associated with widespread manifestations such as strong wind gusts, torrential rainfall, very frequent lightning activity, and large temperature fluctuations. On June 14, a cold front characterized by more persistent precipitation passed over Central Europe.

Figure 4 shows the average 10-min measurement recorded at the Institute of Atmospheric Physics (IAP) surface weather station. The records show the passage of three cold fronts within 48 h. The first most significant cold front passage occurred on 13 July at 19:00 UTC. It was characterized by a dramatic shift in wind and temperature, as well as heavy rain associated with thunderstorm activity. The temperature decreased by 7°C in 1 hour. At the same time, the pressure rose sharply by 6 hPa. The wind shifted from a southeasterly to westerly direction, and a wind gust of 8 ms⁻¹ occurred. Subsequent fluctuations in pressure and wind speed (between 19:00 and 22:00 UTC on 13 July) indicate the existence of a storm activity on the cold front. (The sudden drop in temperature and pressure is due to a “downburst”—that is, a downward flow of cold air and precipitation at the front of a dissipating storm phase. A downburst brings cold air from the upper troposphere to the surface.) The second clear evidence of a storm event illustrated by both pressure fluctuations and precipitation in the morning hours on 14 July was related to

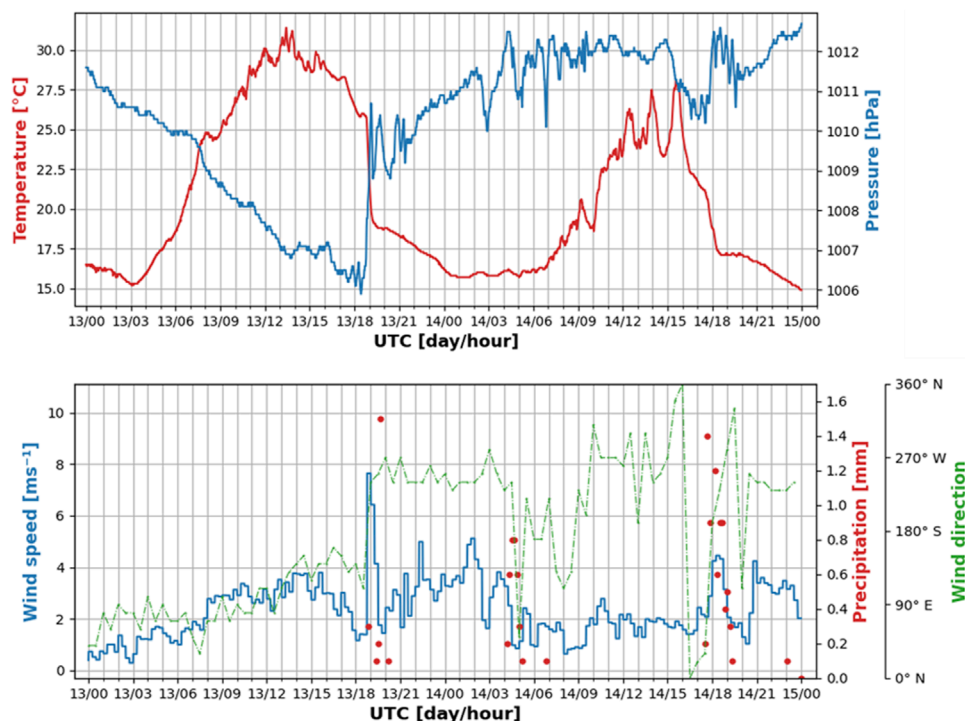


FIGURE 4

Meteorological data recorded at the IAP ground weather station on 13–14 July. The upper panel shows the course of atmospheric pressure and air temperature, and the bottom panel represents wind speed, wind direction, and precipitation (red circles). Sudden changes in atmospheric parameters indicate the passage of the frontal system above the measurement site. Atmospheric pressure, air temperature, and precipitation are measured at 2 m, while wind speed and direction are measured 10 m above the surface.

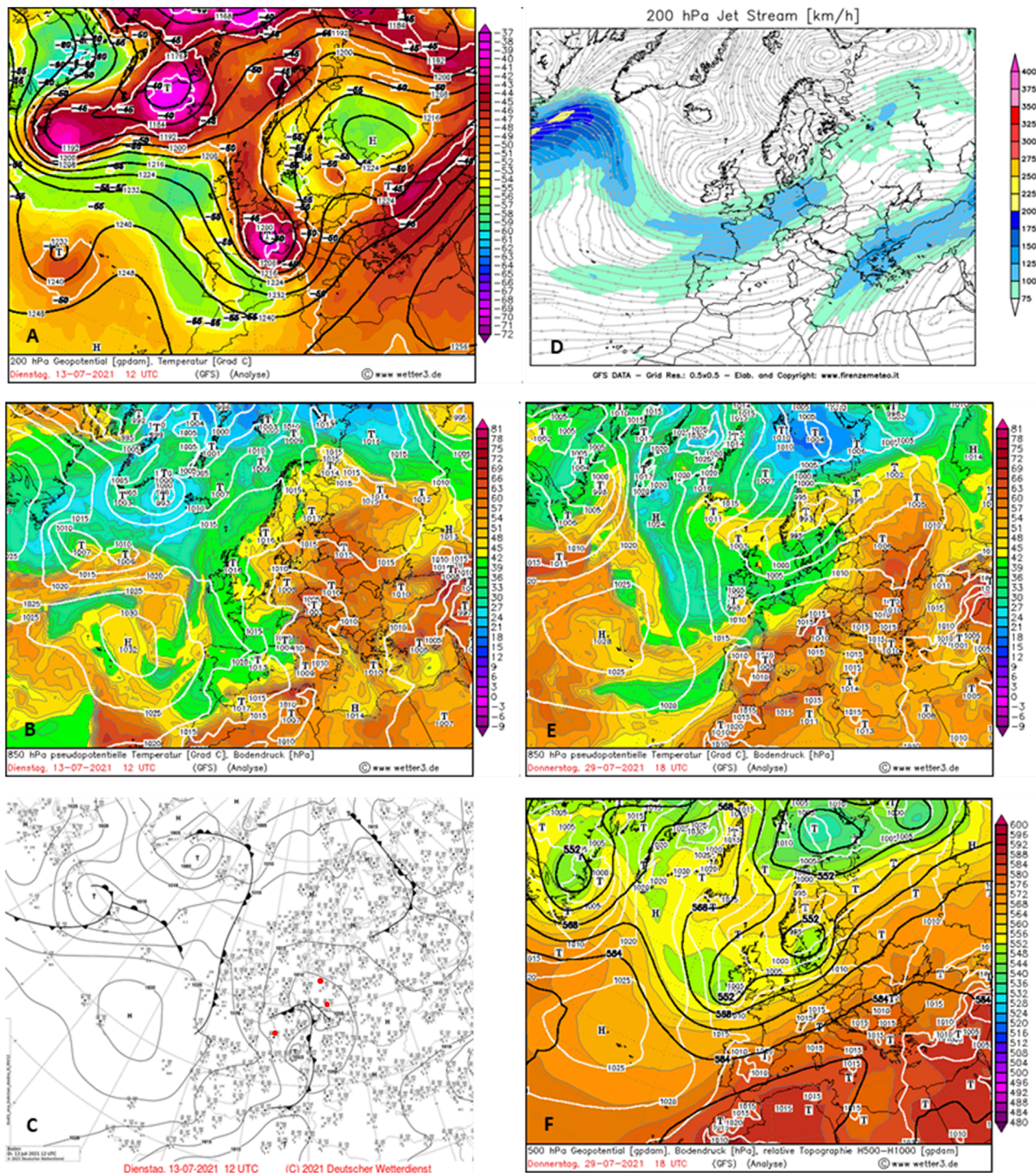
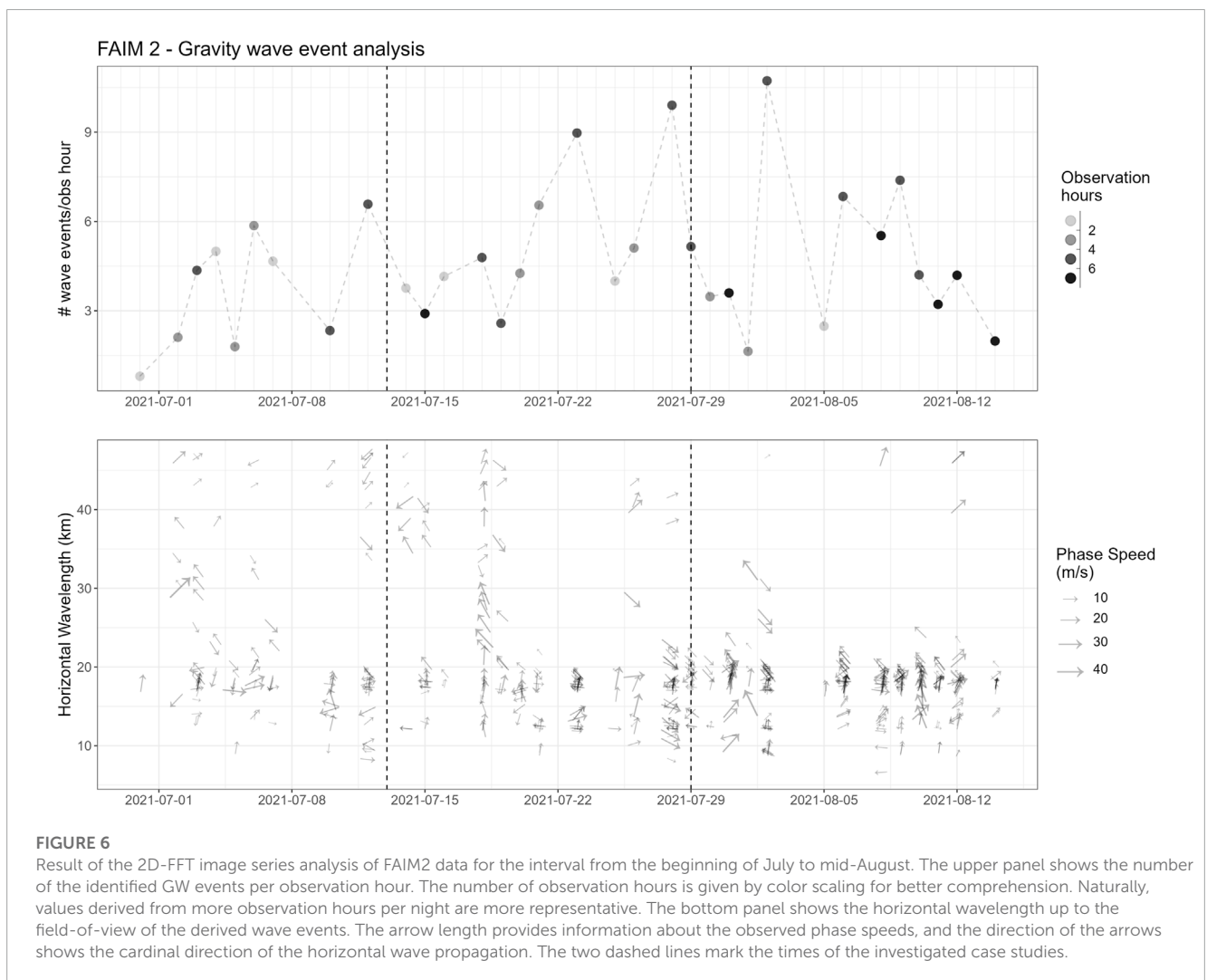


FIGURE 5

Panels in the left column refer to thermal convection on 13–14 July, and panels in the right column refer to orographically driven convection on 29 July. The analyses are valid for 13 July 2021 at 12:00 UTC and 29 July 2021 at 18:00 UTC, respectively. Panel (A) shows the geopotential height of the 200 hPa level (black contours, decameter) and temperature at a 200 hPa pressure level (color scale and white contours). Panels (B, E) show pseudo-equivalent potential temperature at the 850 hPa pressure level (color scale) and sea-level pressure (white contours). Panel (C) shows sea-level pressure with analysis of fronts and air pressure systems, where the letter H/T describes the high/low air pressure centers. The red points indicate the location of Berlin, Prague, and Paris. Panel (D) shows jet stream (color scale) and wind speed and direction (gray contours with arrows) at the geopotential height of the 200 hPa level. Panel (F) shows geopotential height of the 500 hPa level (black contours, decameter), sea-level pressure (white contours), and relative topography between 500 and 1,000 hPa (color scale)—represents the vertical distance between the 1,000 hPa (surface) and 500 hPa (middle troposphere, approximately 5.5 km) levels and varies with temperature and moisture (it is a function of the average virtual temperature). Thus, the color scale regions are directly related to the mean temperature and moisture of the middle troposphere (orange/red values indicate tropical air mass, and yellow/green indicate polar air mass).



the passage of a cold front at 4:00 UTC. The third cold front passed on 14 July at 17:00 UTC and was manifested by a local drop in atmospheric pressure, a sharp decrease in temperature of 5° per hour, and relatively more persistent stratiform precipitation.

On the surface air map, we can see two cyclones with a central pressure of 1,010 hPa located over southeastern France and the Czech Republic (Figure 5C). The position of the waving cold front on the surface pressure field corresponds to the zone with the strongest gradient of pseudo-equivalent potential temperature, θ_{ep} (Figure 5B). The center of the cyclone over the Czech Republic is also an area of local maximum θ_{ep} , i.e., an area with extremely high temperature and humidity in the middle troposphere. High θ_{ep} values at 850 hPa indicate a mid-troposphere instability. In the Czech Republic, θ_{ep} values above 60°C at 850 hPa are rarely reached (only on a few summer days per year), while values above 70°C are very rare, reflecting the presence of very warm and humid tropical air. In the warm sector of the cyclone, a squall line (quasi-linear convective storm system) formed ahead of the cold front, indicated by the twig-shaped line on the surface pressure field map. The upper level weather chart of 200 hPa at an altitude of approximately 12.2 km (Figure 5A) shows that the center of the massive cyclone

over France is located almost in the same place as on the surface (Figure 5C). The exit (northeastern) part of this cyclone extends into an upper-level divergence zone located over the Czech Republic. Divergence in the upper troposphere helps deepen the cyclone and associated convection in the lower and middle troposphere. Both convection, which occurs throughout the vertical extent of the troposphere, and very unstable hot and humid air are the ingredients for the explosive development of storm systems.

4.1.2 Jet stream by orography on 29 July 2021

Weather in Central Europe is influenced by dominant frontal cyclones over Scandinavia and the British Isles (Figures 3D–F). On 29 July, a weak ridge of high pressure from the west in the lower part of the troposphere spread into Central Europe. The ridge was formed by the passive flow of relatively cold Atlantic air into areas of intense thermal convection; hence, pressure gradients near the surface became generally weak. The middle and upper troposphere, however, was associated with a well-marked thermal boundary that formed the so-called polar front. This was formed along the southern flank of the dominant cyclones and divided Europe into a cold north and a hot south (as is shown in the upper air charts in Figures 5E, F).

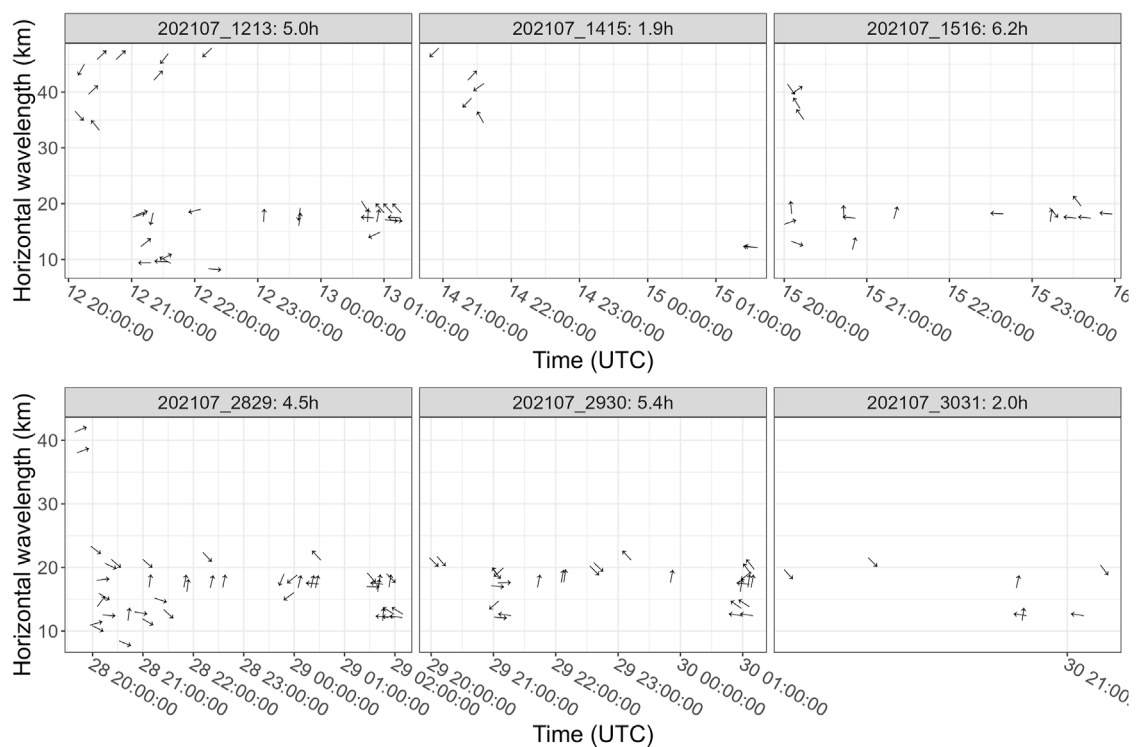


FIGURE 7

Result of the 2D-FFT image series analysis of FAIM2 data. Each arrow shows the gravity wave parameters of a wave event. The arrows show the cardinal directions of horizontal wave propagation (top oriented = north; right oriented = east). The investigated nights and the respective number of observation hours available for analysis are written in the facet titles. The top row is related to the first case study about the thermal convection event, while the second row is related to the second case study.

It should be noted that this polar front was located at an unusually low latitude (in midlatitudes, the polar front tends to occur in spring or autumn).

It is evident from both the upper pressure field maps (Figures 5D, F) and ground pressure isobars (white lines in Figure 5F) that the flow pattern in the troposphere is vertically very homogeneous. The plot of the pseudo-equivalent potential temperature at 850 hPa (Figure 5E) clearly shows the location of a strong polar front in the lower troposphere, separating the cool marine air in the north and northwest of Europe (green color shades) from the moist and very warm tropical air in the rest of Europe (orange and red color shades). The upper air chart of 500 hPa depicts the main flow regime in the mid-troposphere. The relatively small spacing between isohypses at 500 hPa (black lines in Figure 5F) indicates strong horizontal wind speeds in the polar front region.

Figure 5D shows both the wind and position of a jet stream several hundred kilometers wide in horizontal and vertical directions reaching wind speeds of over 125 km/h at 200 hPa. The jet stream usually appears at the location of a narrow transition zone (front) between two air masses with very different temperatures. The axis of the jet stream (the area of maximum wind speed) is near the tropopause. In the summer, the jet stream axis is usually at 200 hPa (approximately 12 km), while in the winter, it is usually at 300 hPa (approximately 9 km) due to the lower temperatures of air mass and hence its higher density and lower tropospheric

thickness. In our particular case, however, the axis of the jet stream is already at approximately 9.3 km above the ground where it reaches a speed of up to 175 km/h over Germany (not shown here). This is significant for the unusually low temperature of the polar air mass for the summer season. We chose the image of the jet stream at 200 hPa because there is a clearly visible area of increased speed over the Ore Mountains in the Czech–German border region. Wind field isotachs show that the wind in the high troposphere was flowing from the southwest along the Ore Mountains. Furthermore, a moderate southwesterly wind (with a speed of approximately 15 km/h) was moving just above the ground. As the wind direction was at an angle of less than 30° to the mountain ridge, no transverse bands of mountain waves were generated as the wind passed around the mountain massif. Moreover, the Ore Mountains are not a monolithic ridge, but there are numerous mountains that pass through the Ore Mountains. In them, the so-called gap wind flowed, where cold air penetrated over the warmer air on the leeward side of the ridge, becoming thermodynamically unstable. Thus, an area of turbulent convective flow was formed over the mountain ridge due to orographic convergence at the surface. Although the humidity was not sufficient to form cumulus clouds and precipitation, increased convection contributed to locally increased wind shear in the evening on 29 July. The wind shear in the jet stream region, enhanced by the aforementioned orographic

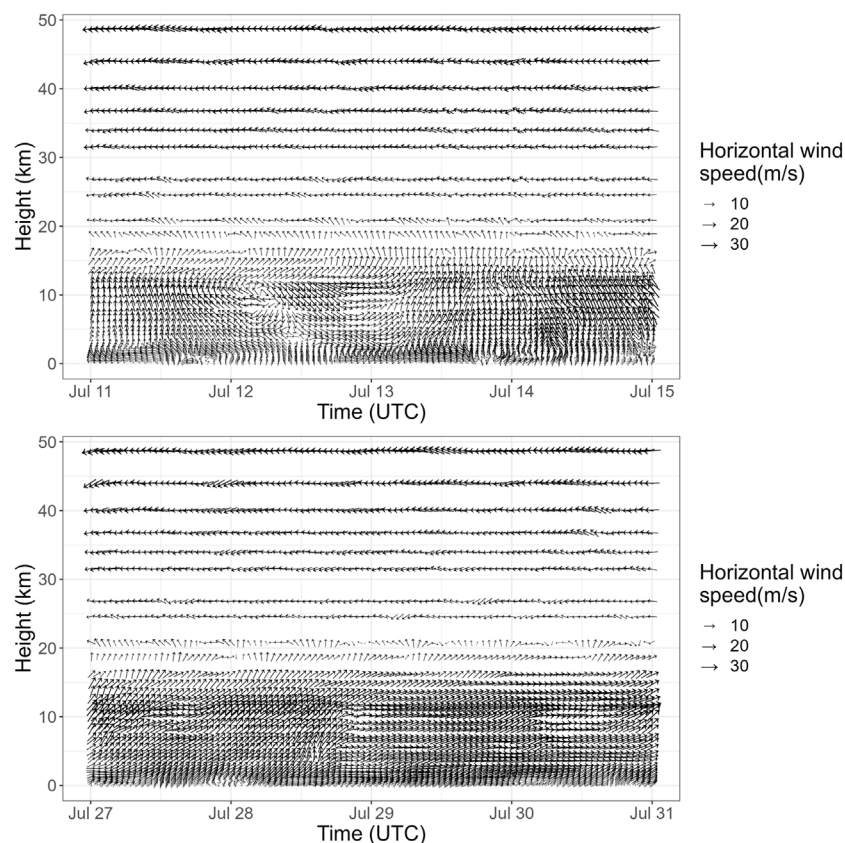


FIGURE 8

Horizontal wind in the troposphere and stratosphere from ERA5 reanalysis data. The orientation of the arrows shows the cardinal directions (top oriented = northward; right oriented = eastward). The top plot is for the first case study, and the bottom plot is for the second case study. Data source: Copernicus Climate Change Service (C3S) (2017). ERA5: Fifth generation of ECMWF atmospheric reanalysis of the global climate. Technical report: Copernicus Climate Change Service Climate Data Store (CDS).

effects, likely led to the fluctuations that were observed in the ionosphere.

4.2 Mesospheric observations

Figure 6 shows the gravity wave activity measured as the number of wave events per observation hour. This metric does not consider the amplitude or duration of the waves but provides some indication about how many different wave signatures (horizontal wavelength and propagation direction) are observed in the mesosphere. The temporal course of this wave activity is characterized by a steady increase until around the beginning of August, only to then decrease again. Superimposed on this steady increase is a modulation of wave activity with a period in the range of approximately 4–6 days. These are typical periods of planetary waves. Planetary waves can interact with gravity waves in various ways due to generation or filtering (see, e.g., Smith, 1996). A more detailed investigation of this possible relation is beyond the scope of this issue. It can be seen that approximately 1 day before the investigated case studies, the gravity wave activity reaches a local maximum. This is larger for the second case study. As mentioned previously, there are also other local maxima of gravity wave activity, e.g., on 23 July and 2 August.

These are not analyzed further as this is beyond the scope of this paper, but comparisons with ERA5 data similar to those performed for the case studies (refer to the following paragraphs) show either wind shear between different height levels or sudden changes in the horizontal wind direction in the troposphere shortly before or around these maxima (not shown here).

Gravity waves generated in the troposphere might be well excited prior to the arrival of the decreased surface pressure front at the Panska Ves Observatory. As they require some time to propagate upward to the mesopause region, which might take up to 24 h, the data are analyzed before, during, and after the events [typical vertical velocities of gravity waves are of the order of 1–3 m/s, see, e.g., Mitchell and Howells (1998)].

Figure 7 shows the wave events for the investigated time periods. The upper row of panels is related to the thermal convection event on 13–14 July 2021. Here, it is remarkable that a majority of waves is observed at the night from 12 to 13th before the cold front reached the Czech Republic (while for the night of 13–14 July, no airglow observations are available due to heavy cloud cover). The waves with larger horizontal wavelengths (30–50 km) propagate to northeast and southwest and are observed at the beginning of the night and continued with smaller-scale waves in different directions. In addition, on 14–15 July, the observed larger-scale waves have an

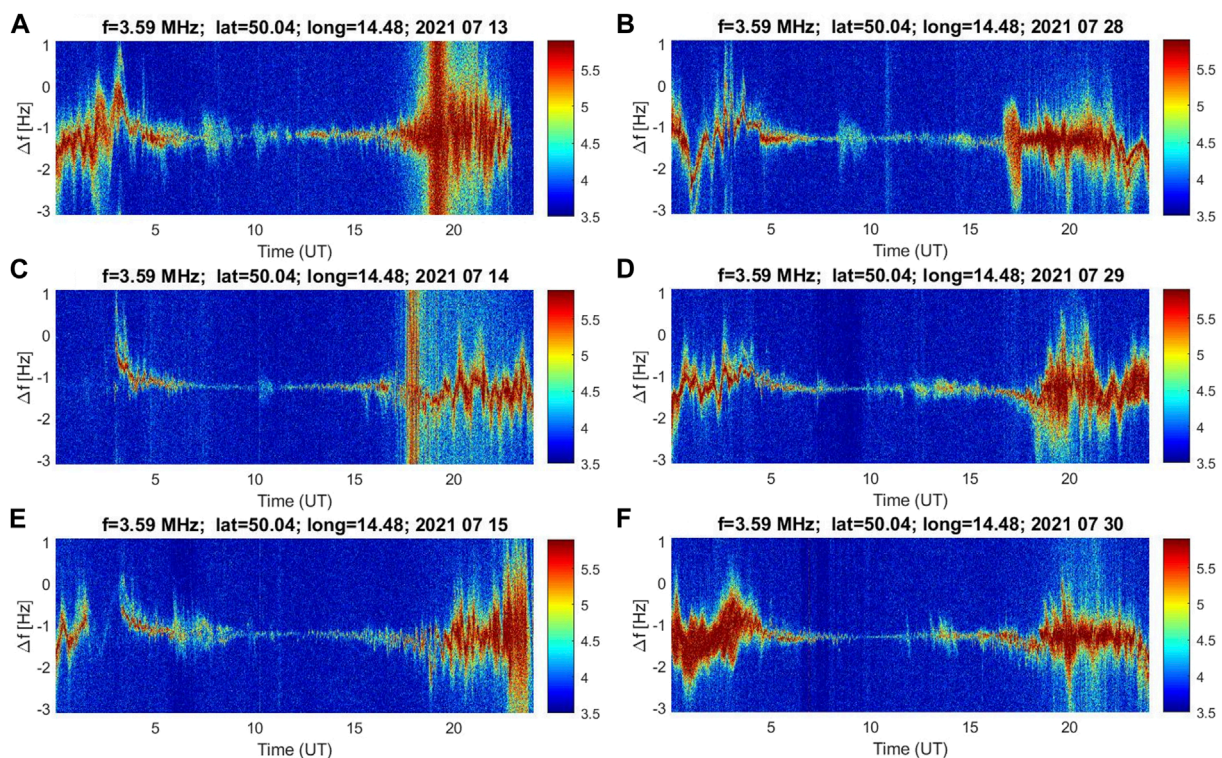


FIGURE 9

CDS spectrograms recorded on several consequent days around the events of interest. Left panels (A,C,E) show measurements during the passage of Bernd cyclone (13–15 July, 2021) while right panels (B,D,F) show the corresponding observation during an orographically driven jet stream situation (28–30 July, 2021). Remarkable noise bands across the whole spectrum are observed in coincidence with frontal passage on 13 and 14 July, which are caused by lightning that occurred near the Doppler receiver. In both cases a relatively broad spectrum associated with the Spread F situation in the ionosphere is registered.

orientation to northeast and southwest and one wave event to the NW direction. This behavior changes during 15–16 July to northwest and southeast and one event to the northeast. A majority of the smaller-scale waves propagates to the northwest and west direction for this night.

Interpreting the propagation directions regarding sources of the gravity waves is difficult. It is well-known that gravity waves are strongly influenced by the environment through which they propagate (e.g., Fritts et al., 2006; Wüst et al., 2017). In particular, one has to consider the effect of wind filtering, i.e., when the wind is in the same direction as the wave propagates, the wave might get filtered depending on its phase speed. On the other hand, wave breaking might itself lead to secondary gravity waves, and wind shear can generate gravity waves as well. In July 2021, the stratospheric wind, which is the most likely reason for wind filtering of waves coming from the troposphere, is westward (see Figure 8, Copernicus Climate Change Service (2017)), and thus we do not expect to see westward propagating (primary) waves which are generated in the troposphere except for very fast waves.

So, if generated by the cold front and thunderstorms on 12 July over Germany, the observed larger-scale waves propagating in the northeast direction should have been able to pass through the atmosphere up to the upper mesosphere and lower thermosphere region and possibly even higher. The source of the observed southwestward propagating gravity waves cannot be in the

troposphere. However, due to a 180° shift, there might be some coincidence with the northeast propagating waves. Even though having carefully checked the results of the Fourier transform analysis and the aggregation to wave events as well as the image data, it might be an analysis issue, leading to a 180° ambiguity. However, there could also be a physical reason for the 180° shift such as wave reflection.

The observed smaller-scale wavelike structures might be instability features of larger-scale waves when they dissipate (i.e., “ripples”) or smaller-scale gravity waves. This cannot be determined by the observations performed here. The tropospheric and lower-stratospheric winds (ERA5 reanalysis horizontal wind data, see Figure 8 top panel) show different orientations of wind shears at the investigated location. We assume that these wind features could lead to small-scale gravity waves in different propagation directions.

At first glance, the gravity waves in the northwest and west directions on 15 July fit well the interpretation that the cold front is emitting those waves which are in the east of the observation site at this time. However, this contradicts the effect of wind filtering. If these waves were generated in the troposphere, they were very likely to be filtered in the stratospheric westward winds. However, the stratospheric winds are relatively weak with only about 20–30 m/s. Another possibility could be that while waves in eastward directions

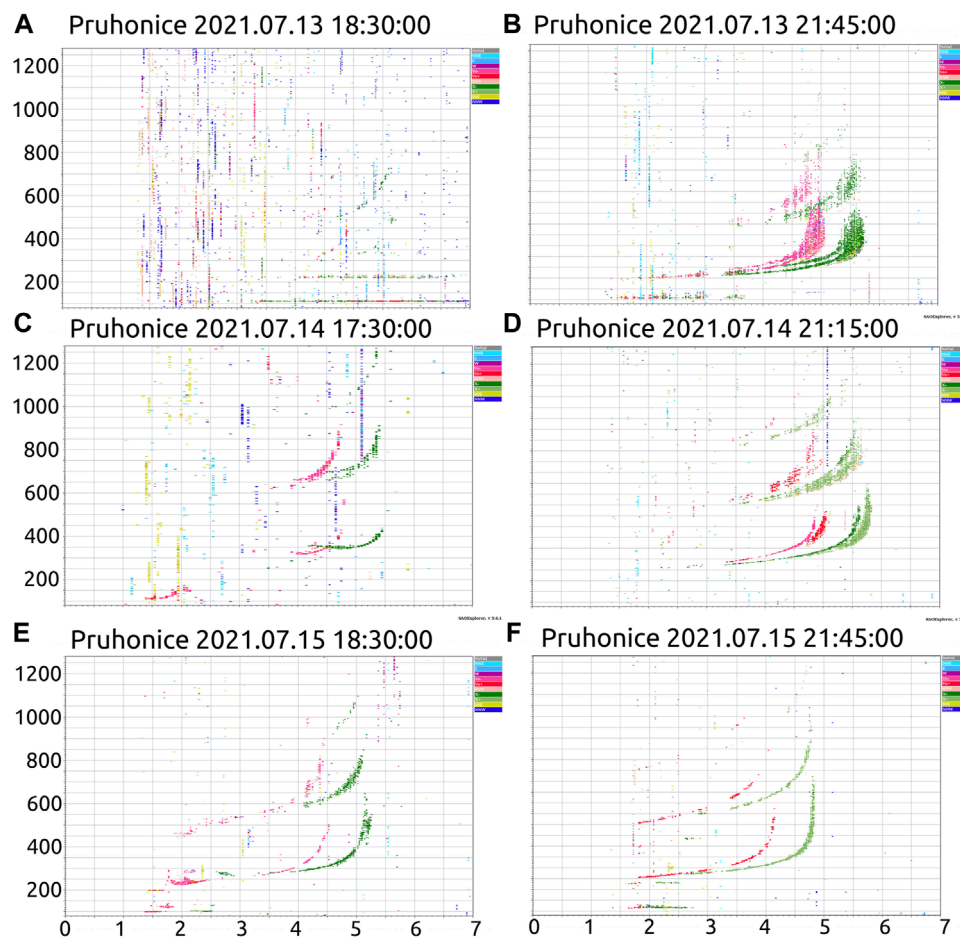


FIGURE 10

Digisonde ionograms in standard representation (horizontal axis shows frequency of the received signal in MHz, while the vertical axis shows height of reflection in km). Vertical ordinary (Vo+ and Vo-) and vertical extraordinary (X+, X-) reflections are denoted in red and green, respectively. Oblique reflections are denoted in blue, magenta, yellow, and pink depending on the direction of reflection. During Bernd cyclone passage above the measurement site, the ionograms recorded by Digisonde are very noisy with strong attenuation of vertical signals (A) and with plenty of off-vertical echo and strong spread-F echo (B). The ionogram (C) is recorded during the passage of the frontal system on 14 July and displays similar features as the preceding frontal passage on 13 July. The ionogram (D) shows that the spread-F echo occurs again, and this example represents a typical ionogram of the night. The spread-F echo is recorded on most ionograms from time intervals (19:00 UTC on 13 July till 5:00 UTC on 14 July and 18:00 UTC on 14 July till 6:00 UTC on 15 July over the ionospheric station Pruhonice). The ionograms (E, F) from time comparable to (A–D) show a normal ionosphere stratification situation with almost only vertical echo.

are emitted by the passed cold front on 15 July, they might emit secondary gravity waves when partially dissipating.

The bottom panel of Figure 7 shows the wave events related to the second investigated event on 29 July. Except for 28 July, no larger-scale waves (within the imager field-of-view of 46 km) are observed; only smaller-scale waves are observed in the range of 10–20 km horizontal wavelength. The number of detected events is the highest in the night from 28 to 29 July with 45 events compared to the 28 events in the night following it and seven events the night after that (but with only two observation hours compared to 4.5 h and 5.4 h). The predominant wave propagation directions are northward and southeastward as well as northwestward during the night from 29 to 30 July.

One might assume a gravity wave source in the south of the observation site and also one in the north on 28 July (or maybe on 27, assuming slowly upward propagating gravity waves), which

could be related to the nearby cold polar front in the north and the warm air in the south as mentioned previously. Interestingly, mainly smaller-scale gravity waves are observed in the upper-mesosphere and lower-thermosphere OH airglow emission.

4.3 Ionospheric observation

4.3.1 Continuous Doppler sounding

Figure 9 shows CDS spectrograms recorded on several consequent days around the events of interest. Spectrogram records reveal substantial differences between the two analyzed cases. Figures 9A, C, E show the Doppler shift spectrograms recorded at 3.59 MHz on the sounding path Panská Ves—Prague from 13 to 15 July 2021. The signal received at night is characterized by a relatively broad spectrum associated with spread F. In addition, two

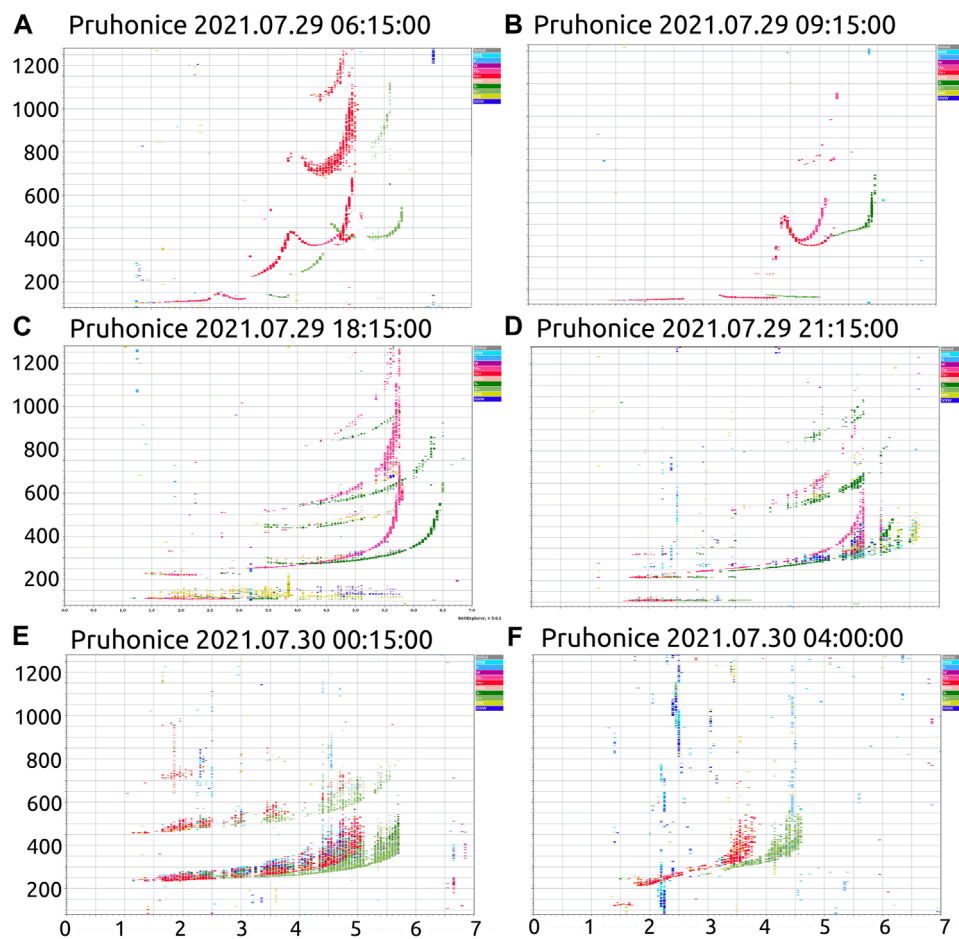


FIGURE 11

Digisonde ionograms as in Figure 10. During the jet stream event, many irregularities were well observed on ionograms. The ionograms (A, B) represent the situation when a cusp occurs on the profile. On the ionograms, there are split echo from the F2 layer. Panels (C, D) show rather good-quality ionograms with well-developed vertical reflections, together with some off-vertical echo. The sporadic E-layer is present on both ionograms. Panels (E, F) represent the spread-F echo that remains till the morning of the following day.

remarkable noise bands across the whole spectrum are observed at approximately 19:00 UTC on 13 July and approximately 18:00 UTC on 14 July. These noise bands consist of many individual vertical lines in the spectrograms and are caused by lightning that occurred near the Doppler receiver. Lightning activity and electrically charged thunderclouds were also observed by the electric field mill located in Panska Ves. The sharp/sudden increase in noise within CDS spectra in time coinciding with the fast moving midlatitude frontal cyclone was reported by Koucká Knížová et al. (2020).

The spectrum broadening of signals associated with spread F is also clearly visible on the spectrograms recorded during jet stream meteorological event from 28 to 30 July, as shown in Figures 9B, D, F. The broadening is the largest in the night during 29–30 July 2021; it is well-pronounced until approximately 04:00 UTC on 30 July. It should be noted in this regard that it is generally believed that acoustic-gravity waves propagating from below may act as a seeding mechanism for the development of spread F (Booker, 1979; Huang et al., 1994; Nicolls and Kelley, 2005).

4.3.2 Digisonde

Panels in Figure 10 show raw ionograms recorded during 3 days, from 13 to 15 July 2021. During the Bernd cyclone passage above the measurement site on 13 July, the ionograms (A) and (B) recorded by DPS-4D are very noisy with plenty of off-vertical echoes. The vertical signal of both ordinary and extraordinary modes is attenuated, especially on ionogram (A). Ionogram (B) represents the situation with the spread-F echo that is recorded on most ionograms of this day. On the middle part, the left ionogram (C) is recorded during the passage of the frontal system on 14 July and displays similar features as ionograms from the previous event. On the right ionogram (D), spread-F echo occurs again and represents a typical ionogram of the night. The spread-F conditions exist during geomagnetically disturbed situations. However, under geomagnetic forcing, the F2 traces are usually deformed, and significant changes in shape (e.g., cups) of the F traces are observed. Contrary to this, the ionograms (A–D) do not differ at first sight from the quiet ionograms by means of shape of the reflection. Therefore, the main deviation from the quiet-time ionograms is the presence of spread-F reflections.

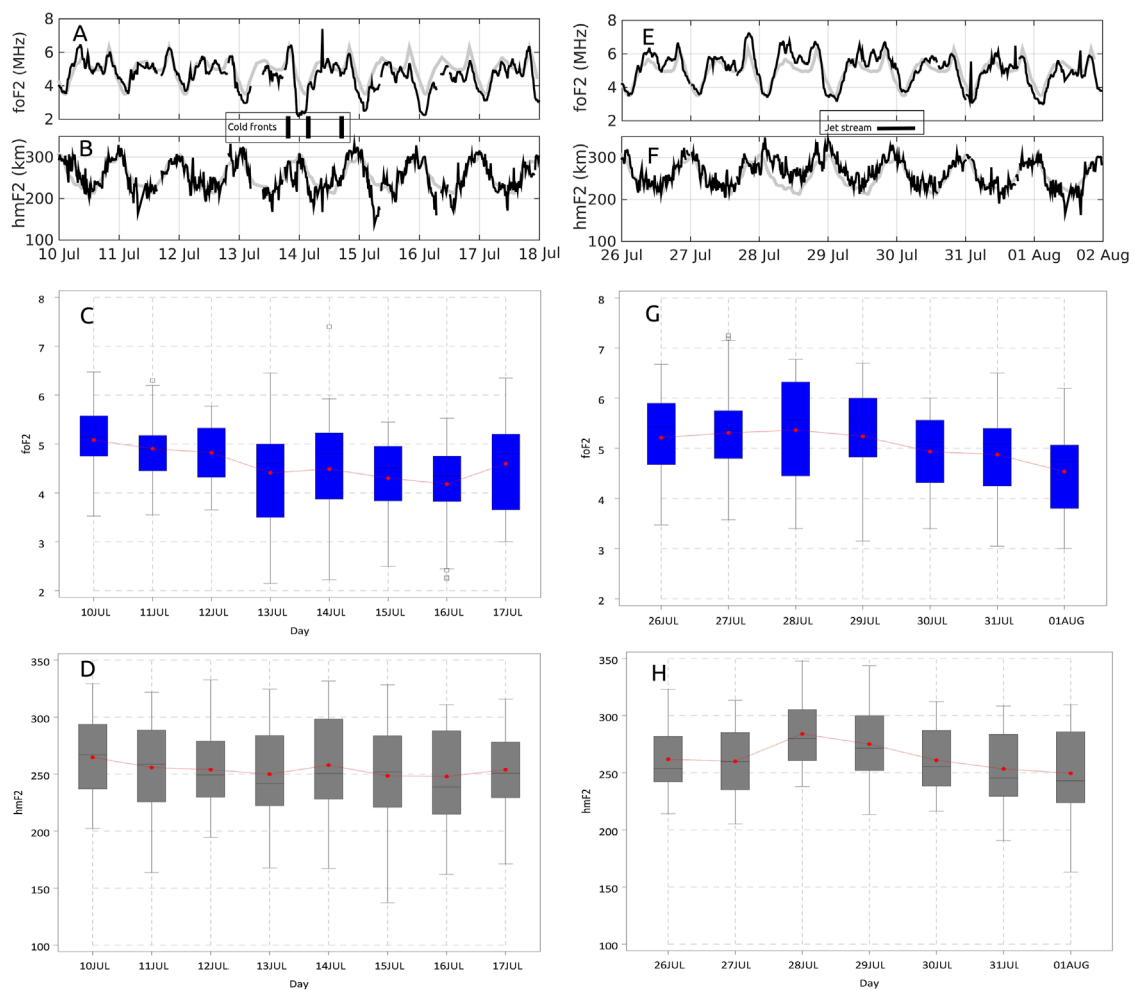


FIGURE 12

Bernd cyclone situation (A–D) and jet stream situation (E–H). Vertical lines in (A, B) denote individual passages of cold fronts, and the horizontal line in (E, F) denotes the period of the jet stream situation. Panels (A, E) show critical frequencies foF2 (black) with median values (gray). Panels (B, F) show peak heights of the F2 region hmF2 with median values. Both time intervals are described using boxplot graphs (C, D) for a convective situation and (G, H) for a jet stream situation. Comparison with monthly median values of foF2 shows that the days 10–13 July match the median values well. A significant decrease in night values of foF2 occurred shortly after the Bernd (A) passage. During daytime, only a slight decrease in noon values of foF2 compared to preceding days can be identified. Critical frequency foF2 during noon hours stayed at lower values for the following 3 days compared to median values and the days prior to the Bernd passage. No significant changes in hmF2 could be well seen (B). Boxplots (C, D) and (G, H) are organized in groups by days. Box and whisker plots display the mean (dot signs), median (horizontal lines in boxes), quartiles (color boxes), outliers (rings), and minimum and maximum observations (whiskers) for data groups. Rather stronger oscillation/variability could be identified on the course of foF2 on 29 July (E) compared to the preceding and following days; however, the general course of the day corresponds roughly to the monthly medians of foF2. A significant increase in hmF2 beginning on 28 July can be observed till 29 July.

As we will show further, changes in foF2 and hmF2 parameters compared to quiet time were observed. Two bottom ionograms from 15 July (E) and (F) show normal ionosphere stratification with almost only vertical echoes, implying that the ionosphere returned to a normal state. As mentioned previously, the spread-F ionograms indicate irregular stratification of the ionosphere. According to our experience (for instance, Koucká Knížová et al., 2021), the presence of atmospheric gravity waves leads to observation of spread-F situations even during periods of rather low geomagnetic activity.

Ionograms given in Figure 11 are related to the jet stream event. They show a large variety of echo types with plenty of irregularities. The first ionogram (A) represents a situation when a cusp occurs on

the profile (the cusp can be observed between 4.8 and 5.2 MHz). On the following ionogram (B), echo from the F2 layer splits into two. Then, ionograms (C) and (D) show irregular stratification at heights of the F1 layer which seems to be split into two sublayers. The further two ionograms (E) and (F) show good quality with well-developed vertical reflections, together with some off-vertical echoes. Such a large variability of ionogram records indicates a rather non-stable situation within the ionosphere that is probably disturbed by the presence of propagating atmospheric waves. In addition to spread-F echo ionograms, the cusp occurrence on the profile also points to the propagating atmospheric gravity waves.

Figure 12 shows the daily course of critical frequency foF2 (on panels A and E) and hmF2 (on panels B and F) measured for 7

consecutive days. Left panels A–D refer to the Bernd event, and right panels E–H show the jet stream situation. During 11 and 12 July the foF2 shows regular course, it means the increase of foF2 during daytime due to direct solar ionization and decrease of foF2 with decreasing amount of solar radiation to night values, when due to recombination processes only low ionization remains at F2 layer. The asymmetry in the maximum of foF2, which is shifted toward afternoon hours rather than to the time of minimum zenith angle at noon (time of maximum ionization), is well-documented phenomena attributed to recombination processes (see, for instance, Davies, 1990). A rather interesting feature on 13 July is a sharp decrease in foF2 after 18:00 UTC with respect to preceding days. In general, the foF2 stays a bit lower for the following 3 days and starts to rise again on 18 July. Correspondingly, the height hmF2 slightly decreases for a few days. It indicates that the whole profile of electron concentration is moved downward and remains there for several days. It is important to point out that during all studied days of convective events, the height of the layer maximum

(Figure 12B) is lower than during the following orographically driven convective situation in the jet stream zone (Figure 12F). In addition to that, on the course of hmF2, less variability could be observed during the later event showing, at first glance, a much more regular course. However, a small decrease in the whole profile can be observed beginning on 29 July. On the course of foF2, as shown in Figure 12E, one can notice a decrease in the critical frequency foF2 during days 30 and 31 July for daytime. The difference in night time values can be observed between 29/30 July compared to 31 July/01 August and 01/02 August; however, a slight decrease in night foF2 is also observed compared to the nights of 25/26–29/30 July.

The boxplot procedure indicates a significant departure of the foF2 and hmF2 diurnal course from normal behavior. Figures 12C, D, G, H show statistical boxplots of foF2 and hmF2. Plots are organized in groups by days. Box and whisker plots display the mean (dot signs), median (horizontal lines in boxes), quartiles (color boxes), outliers (rings), and minimum and maximum

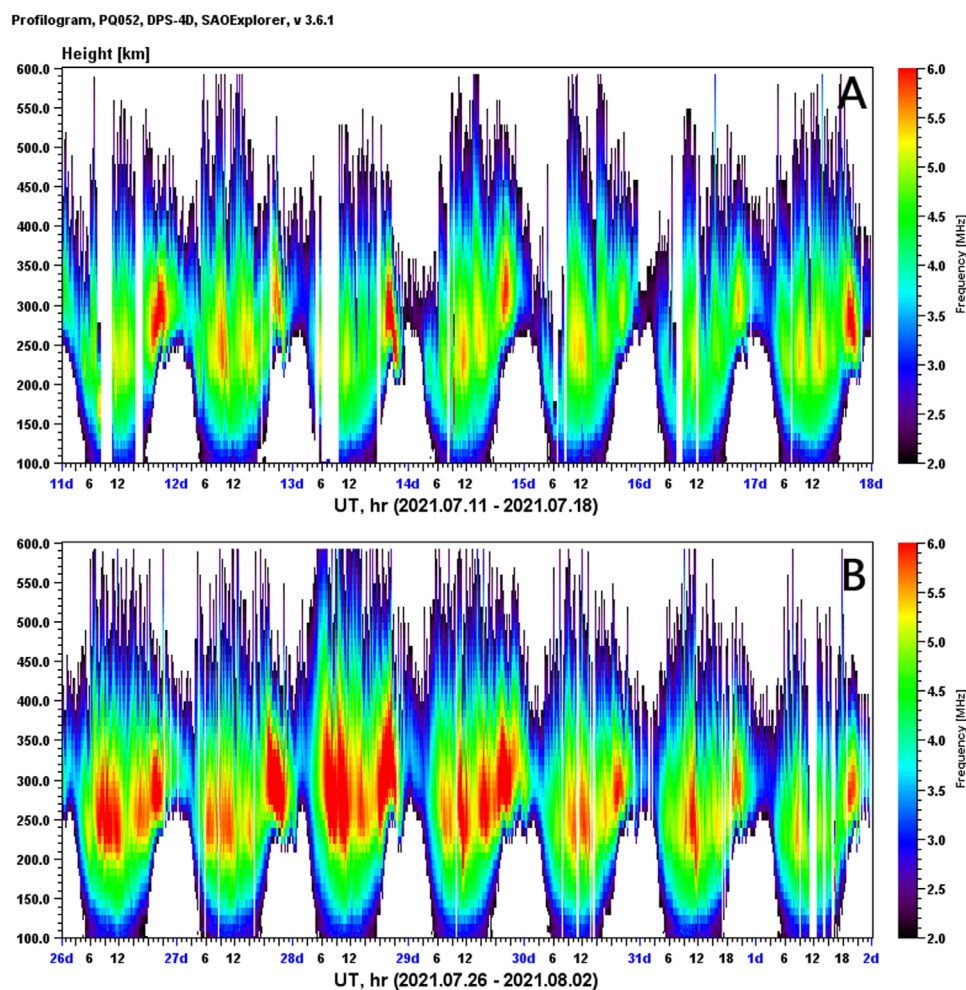


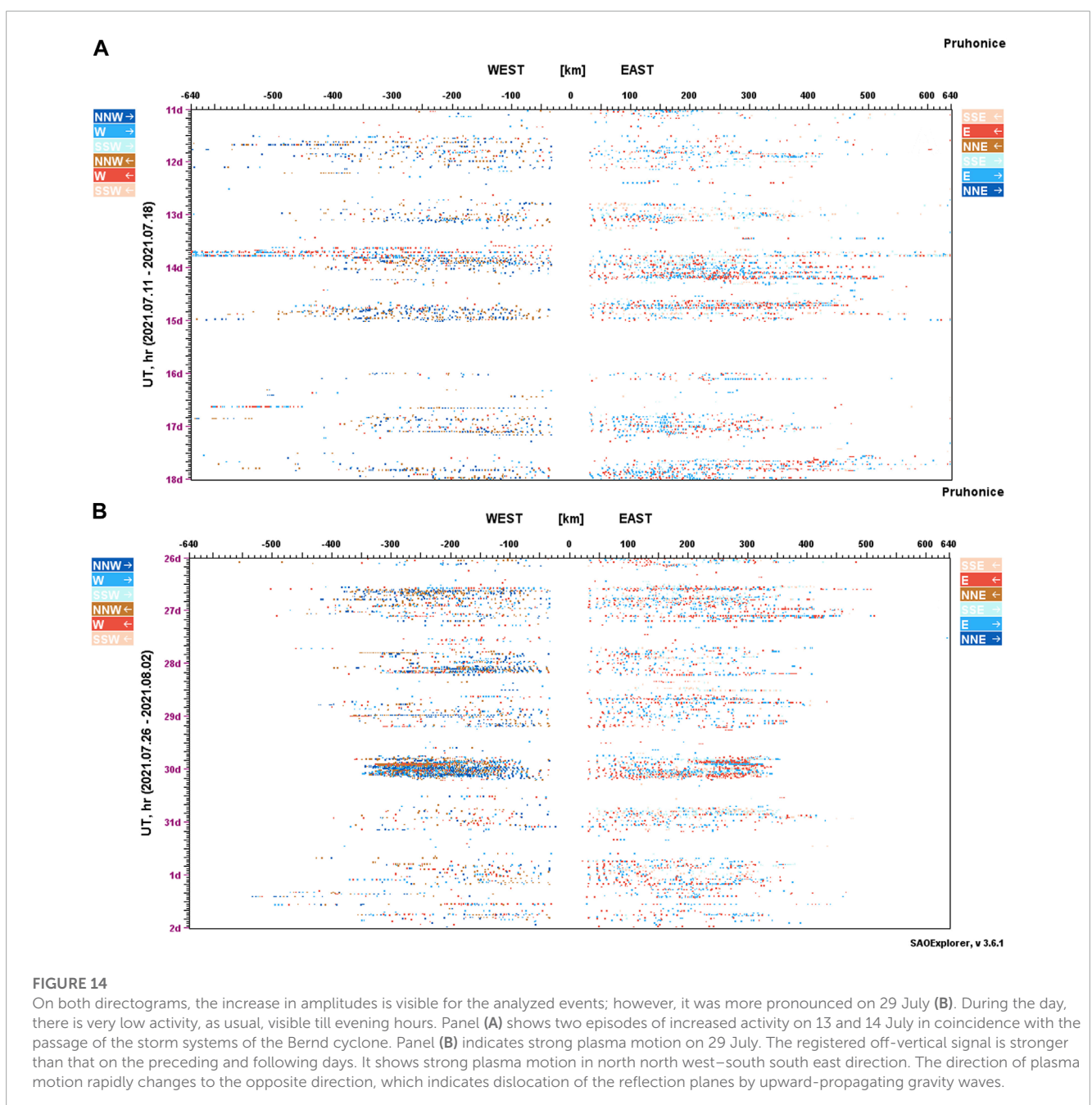
FIGURE 13

Profilingrams obtained from full electron concentration profiles (ionograms are manually scaled, and the NHPC inversion method within the SAO explorer is applied) for a Bernd event (A) and jet stream (B). Profilingrams indicate that ionization within the whole F-layer ionosphere is higher during the jet stream event on 29 July (B) than ionization around mid-July (A). In both cases, oscillations in the gravity wave domain are well observed during the entire studied time span.

observations (whiskers) for data groups. Figure 12C shows a substantial change in the foF2 distribution. The mean value remains lower than the median value till the end of the analyzed term. Figure 12D shows a difference in the mean and median values for the entire observation time; the largest difference is visible on 13 and 14 July. Furthermore, plots in Figures 12G, H show the same analyses for the orographically driven convection in the jet stream zone event. Contrary to the thermal convection event, mean and median values differ consistently for the entire monitored time. The median value stays higher than the mean value of foF2, while the median value remains smaller than the mean value of hmF2. However, the largest difference in the case of foF2 is observed on 29 July, while for hmF2, the difference starts to increase on 30 July. The deformation of the

diurnal courses of the main ionospheric parameters in both analyzed cases is probably linked to the increase in AGW activity within ionospheric heights with the origin in tropospheric situations. Wavelet transform analysis applied on foF2 and hmF2 reveals an increase in power on oscillation periods 30 min and 1–3 h and approximately 3 h on 13/14 July and on periods 3–4 h on 29 July. Oscillations are better pronounced within foF2.

Profilograms in Figure 13 show the variation in profiles during several consequent days around the studied events. Gaps are caused by the presence of a sporadic E-layer which partially or fully prevents the sounding signal from reaching upper laying layers. However, scaling of the main parameters, foF2 and hmF2, could still be possible when the blanketing frequency is lower than the critical



frequency of the F-layer. Accuracy of the electron density profile scaling or main parameters foF2 and hmF2 is affected by the spread-F echo or cusps present on the profile.

On both panels of Figure 13, the Bernd cyclone on panel (A) and jet stream event (B), there are visible wavelike oscillations of the entire profile in the period range of gravity waves with periods of approximately 3 h observed in a regular increase and decrease in the detected plasma frequency. The estimation is qualitative due to limitations in profile scaling. The ionization level observed during the observation time of the Bernd cyclone passage event is lower during the entire monitoring period of the orographically driven convection in the jet stream zone. In agreement with foF2 courses given in Figure 12, the ionization decreases in the entire profile after the Bernd cyclone passage (Figure 13A) and jet stream event (Figure 13B).

On both directogram plots (Figure 14), the increase in echo amplitudes is well-visible for both analyzed cases. During the quiet daytime period, there is very low activity visible on the directograms till the evening hours. Figure 14A shows two episodes of increased activity on 13 and 14 July in coincidence with the passage of the

storm systems of the Bernd cyclone. The DPS 4D antenna system registers variable signals and detects the quickly changing direction of the plasma motion. On the night of 13/14 July, the detected plasma flow and shears appeared first in east-west (EW) direction and were later observed in the north northwest–south southeast (NNW–SSE) direction. On 14/15 July, in the night, the plasma flow and shears were detected almost only in the NNW–SSE direction. Figure 14B shows strong plasma motion on 29 July. The registered signal is substantially stronger than that on the preceding and following days. It shows strong plasma motion in the NNW–SSE direction. The direction of plasma motion rapidly changes into the opposite direction.

The increased Doppler echo can indicate both increase in the plasma flow in the horizontal direction and substantial changes in the undulation of reflection planes. The direction of the registered plasma flow quickly changes to the opposite direction, which confirms that the reflection planes are probably disrupted by the propagation of atmospheric waves with both horizontal and vertical components.

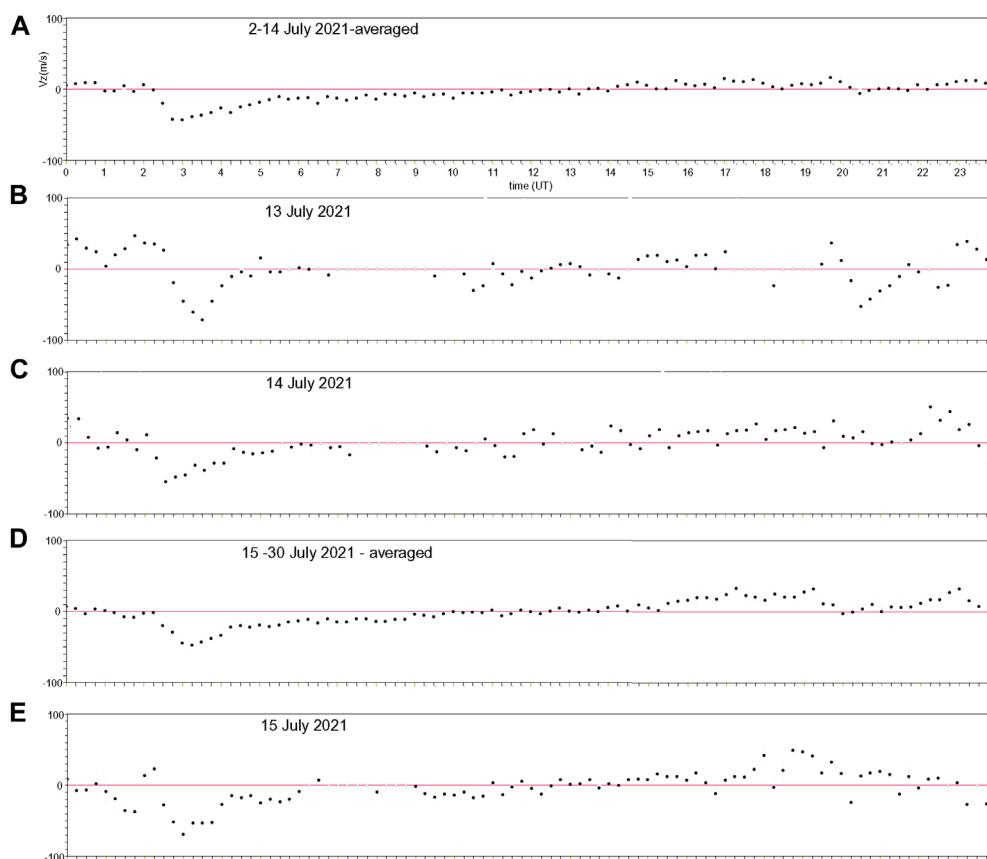


FIGURE 15

Occurrence of sporadic E does not allow the determination of plasma drift velocity during whole days of interest. On 13 July (B) shortly after the frontal passage, strong opposite plasma flow was detected. It was followed by a less pronounced morning downward peak on 14 July compared to the averaged values of the reference time span (A). On 14 July (C) after the second frontal passage, higher values of plasma were observed than those in the reference diurnal course. On the course of the vertical component of plasma drift, rather high variability during the whole day can be observed (E). In the morning hours, a short episode of opposite plasma motion appears. The morning downward peak is less pronounced compared to the reference time span. During evening hours, larger values of the drift are recorded with respect to the reference course. During evening hours, the vertical component significantly changes the direction. Drift course data are compared to averaged values for the reference time span of 5 days preceding the event (D).

As mentioned previously, the occurrence of sporadic E does not allow the determination of all ionospheric plasma properties for all ionograms, and the plasma drift velocity cannot be computed for whole days of interest. However, qualitative interpretation of the vertical plasma drift component (Figure 15) is still possible. Drift data recorded during days of events are compared to averaged values obtained for 5 days preceding the event. On 13 July, shortly after the frontal passage, strong opposite plasma flow was detected (Figure 15B) with respect to the reference day (Figure 15A). It is followed by a less pronounced morning downward peak on 14 July (Figure 15C) compared to the reference behavior. On 14 July, after the second frontal passage, plasma flows in the same direction as on the reference day. Somewhat higher values of plasma were observed compared to the reference diurnal course.

On the course of the vertical component of plasma drift, (Figure 15E) rather high variability during the whole day can be seen apparently. In the morning hours, a short episode of opposite plasma motion appears. The morning downward peak is less pronounced than the reference diurnal course (Figure 15D). In evening hours, larger values of the drift are recorded with respect to the reference course. In addition to that, the vertical component significantly changes the direction in the afternoon hours and mainly during evening hours.

5 Conclusion

We analyzed two tropospheric mesoscale situations caused by exceptional synoptic-scale circulation conditions enhanced by the influence of the local convective environment. The first situation represents changes induced by convective upward motions in the squall line ahead of a cold front with heavy rainfall on 13–14 July 2021 (Bernd cyclone). The second situation describes induced effects of the polar front jet stream in the upper troposphere enhanced by orography with an atypical location of the jet stream on 29 July 2021. These two selected tropospheric situations evolved during rather low and stable solar and geomagnetic conditions ($F_{10.7_{\text{mean}}} = 81.06$ and $F_{10.7_{\text{median}}} = 77.65$; $Kp_{\text{mean}} = 1.26$ and $Kp_{\text{median}} = 1$). Therefore, we expect that the observed perturbations within ionospheric plasma are of neutral atmosphere origin. Geomagnetic activity increased only for two short episodes classified as moderate. Using meteorological, mesosphere, stratosphere, and ionosphere data, we identified tropospheric disturbances and further detected and analyzed possible induced effects through the atmosphere up to the ionospheric F2 region. Due to the coincidental occurrence of the observed variability within the mesosphere and ionosphere, we attribute the resulting ionospheric disturbances to the neutral lower-atmosphere forcing rising from the discussed tropospheric situations.

We identified substantial changes in the behavior of particular atmospheric parameters in time coherence with observed meteorological situations. Our main observational findings are summarized as follows:

1. Spread-F echo occurs after the frontal passage on CDS spectra and DPS 4D ionograms.
2. Spread-F echo develops in connection with orographically enhanced jet stream on CDS spectra and DPS 4D ionograms.
3. Irregularities (cusps, layer splitting, and spread F) occur on ionograms related to orographically enhanced jet stream.
4. Distortion of diurnal foF2 and hmF2 distributions is observed during both analyzed events.
5. Wavelike oscillation in the GW mode develops in ionospheric parameters, in particular, on profilograms.
6. Increase in the detected amplitude of horizontal plasma flow is registered during event days.
7. Qualitative changes in the vertical plasma drift during the studied days are recorded with respect to the reference time.
8. Increase in GW activity in the mesosphere is detected before and around the analyzed events. Stronger activity is observed in connection with orographically enhanced jet stream, likely due to cloud coverage.
9. A majority of waves observed in the mesosphere occur during the night before the cold front reaches the observational point.
10. Identified GW structures in the mesosphere propagate into a wide range of directions, and no prevailing direction can be identified.
11. Large-scale and small-scale GW structures are observed in the mesosphere during Cyclone Bernd.
12. Only small-scale GW structures are registered in the mesosphere in relation to the jet stream situation.

As mentioned previously, the study involves selected events observed during the time of low solar activity and low-to-moderate geomagnetic activity; hence, we consider it correct to attribute most of the observed ionospheric variability to the sources within the lower-lying neutral atmosphere. In our cases, we assume that the waving frontal boundary (Cyclone Bernd) and boundary of air masses with a sharp temperature gradient (polar front jet stream situation) may act as an effective source of the gravity waves that propagate as high as the F2 ionospheric region. Certainly, due to the presence of winds, part of the launched gravity wave spectra may be filtered out without reaching the ionosphere. However, part of the observed gravity wave activity may be caused by the secondary waves due to primary wave breaking.

Our study suggests that the observed larger-scale gravity waves, seen within mesospheric and ionospheric data, can be generated by the movement of the frontal system of the continental scale. Large-scale GW structures are completely missing in the mesospheric observations in the case of a polar jet stream event. In both analyzed cases, we observe small-scale GW structures within mesosphere airglow data.

Our investigation shows the possible link between the source meteorological systems that effectively launch the atmospheric waves that propagate upward through the mesosphere up to ionospheric heights where they influence the general state of neutral atmosphere and also due to coupling ionospheric plasma. The observed mesospheric and ionospheric response to the initial meteorological situations shows some differences. Airglow measurement seems to be sensitive to GW detection that very likely

originates from an atypically located jet stream and intensive frontal systems.

The observed departures from the regular ionospheric behavior account for the fact that the forcing from the lower-lying atmospheric regions should not be neglected and may form an important part of the observed variability and a substantial part of the day-to-day variability under stable solar forcing. The CDS spectrograms seem to be an effective and instant tool for the detection of AGW-induced disturbances in the ionosphere associated with moving frontal systems.

For additional requirements for specific article types and further information please refer to “Article types” on every Frontiers journal page.

Data availability statement

The datasets presented in this study can be found in online repositories. The names of the repository/repository and accession number(s) can be found at: Geomagnetic Data Center: <https://www.gfz-potsdam.de/en/>; Meteorodata: <https://www.wetterkontor.de/de/wetterlage.asp#erlaeuterungen>, <https://www1.wetter3.de/Archiv/https://www.firenzemeteo.it/maps/mappe-previsioni-meteo-gfs.php>, <https://weather.uwyo.edu/upperair/sounding.html>, <https://www.ufa.cas.cz/en/stanice-praha-sporilov-2/>; Ionosphere: https://www.ufa.cas.cz/DATA/files/oia/Doppler_des_365.pdf, <http://datacenter.ufa.cas.cz/>, <http://giro.uml.edu>; Mesosphere: FAIM2 data are stored in the World Data Center for Remote Sensing the Atmosphere (WDC-RSAT). Data available on request. Copernicus Climate Change Service (C3S) (2017). ERA5: Fifth generation of ECMWF atmospheric reanalysis of the global climate. Technical report, Copernicus Climate Change Service Climate Data Store (CDS). For the scaling of raw ionogram Software SAO Explorer: <https://ulcar.uml.edu/SAO-X/SAO-X.html>.

Author contributions

PK analyzed Digisonde data, performed analyses, provided interpretation, prepared the review part, and wrote the first draft of the paper. KP analyzed tropospheric flow dynamics and classified meteorological situations and wrote the meteorological part of the manuscript. KP analyzed Digisonde data and performed statistical analyses. JC operated CDS, analyzed data, and provided interpretation. ZM analyzed Digisonde data and provided interpretation. DK operated Digisonde, prepared campaigns, analyzed Digisonde data (drifts), and provided interpretation. The analysis methods for the FAIM data (mesospheric part of the

manuscript) were developed by PH supported by SW and MB within the project VoCaS-Alp. PH analyzed the FAIM data for this manuscript. Together with SW and MB, he interpreted them and wrote the corresponding part of the manuscript. JK substantially contributed to the synoptic evaluation and interpretations of meteorological events. All authors contributed to the article and approved the submitted version.

Funding

Part of the data collection and analyses of the IAP team was performed under the support of H2020-INFRAIA-2018-2020 PITHIA-NRF (Grant Agreement Number: 101007599) and Project HORIZON-CL4-2022-SPACE-01101081835 T-FORS. Work of KPod was partly supported under the grant GA21-03295S by the Czech Science Foundation, and work of JC was supported by the Mobility Project of the Academy of Sciences CONICET-22-02. The analysis methods for FAIM data were developed within the project VoCaS-ALP which received funding from the Bavarian State Ministry of the Environment and Consumer Protection under Grant No. TKP01KPB-70581. Both teams acknowledge the HR Project Development of Research and Development Capacities at the Institute of Atmospheric Physics CAS (Project Reg. No. CZ.02.2.69/0.0/0.0/18_054/0014500).

Acknowledgments

The authors would like to thank Josef Boška, who passed away before completing the manuscript, for his advice and suggestions.

Conflict of interest

The authors declare that the research was conducted in the absence of any commercial or financial relationships that could be construed as a potential conflict of interest.

Publisher's note

All claims expressed in this article are solely those of the authors and do not necessarily represent those of their affiliated organizations, or those of the publisher, the editors, and the reviewers. Any product that may be evaluated in this article, or claim that may be made by its manufacturer, is not guaranteed or endorsed by the publisher.

References

- Bauer, S. (1958). An apparent ionospheric response to the passage of hurricanes. *J. Geophys. Res.* 63, 265–269. doi:10.1029/JZ063i001p00265
- Bencze, P., and Bakki, P. (2002). On the origin of mid-latitude spread-F. *Acta Geod. geoph. hung.* 37, 409–417. doi:10.1556/AGeod.37.2002.4.4
- Berdermann, J., Kriegel, M., Banyś, D., Heymann, F., Hoque, M. M., Wilken, V., et al. (2018). Ionospheric response to the X9. 3 flare on 6 September 2017 and its implication for navigation services over Europe. *Space weather.* 16 (10), 1604–1615. doi:10.1029/2018SW001933
- Bertin, F., Testud, J., Kersley, L., and Rees, P. R. (1978). The meteorological jet stream as a source of medium scale gravity waves in the thermosphere: An experimental study. *J. Atmos. Terr. Phys.* 40, 1161–1183. doi:10.1016/0021-9169(78)90067-3

- Bishop, R. L., Aponte, N., Earle, G. D., Sulzer, M., Larsen, M. F., and Peng, G. S. (2006). Arecibo observations of ionospheric perturbations associated with the passage of tropical storm Odetta. *J. Geophys. Res.* 111, A11320. doi:10.1029/2006JA011668
- Blanc, E., Farges, T., Le Pichon, A., and Heinrich, P. (2014). Ten year observations of gravity waves from thunderstorms in Western Africa. *J. Geophys. Res. Atmos.* 119, 6409–6418. doi:10.1002/2013JD020499
- Booker, H. G. (1979). The role of acoustic gravity waves in the generation of spread-F and ionospheric scintillation. *J. Atmos. Terr. Phys.* 41, 501–515. doi:10.1016/0021-9169(79)90074-6
- Borchevskina, O., Karpov, I., and Karpov, M. (2020). Meteorological storm influence on the ionosphere parameters. *Atmosphere* 11, 1017. doi:10.3390/atmos11091017
- Borries, C., Berdermann, J., Jakowski, N., and Wilken, V. (2015). Ionospheric storms—a challenge for empirical forecast of the total electron content. *J. Geophys. Res. Space Phys.* 120 (4), 3175–3186. doi:10.1002/2015JA020988
- Boška, J., and Šauli, P. (2001). Observations of gravity waves of meteorological origin in the F-Region ionosphere. *Phys. Chem. Earth Part C.* 26 (6), 425–428. doi:10.1016/S1464-1917(01)00024-1
- Bowman, G. G. (1990). A review of some recent work on mid-latitude spread-F occurrence as detected by ionosondes. *J. Geomag. Geoelectr.* 42, 109–138. doi:10.5636/jgg.42.109
- Bowman, G. G., Dunne, G. S., and Hainsworth, D. W. (1987). Mid-latitude spread-F occurrence during daylight hours. *J. Atmos. Terr. Phys.* 49, 165–176. doi:10.1016/0021-9169(87)90051-1
- Bowman, G. G. (1988). Small-scale stratifications associated with daytime travelling ionospheric disturbances in mid-latitude regions. *Ann. Geophys.* 6, 187–194.
- Bowman, G. G. (1981). The nature of ionospheric spread-F irregularities in mid-latitude regions. *J. Atmos. Terr. Phys.* 43, 65–79. doi:10.1016/0021-9169(81)90010-6
- Buonsanto, M. J. (1999). Ionospheric storms—A review. *Space Sci. Rev.* 88, 563–601. doi:10.1023/A:1005107532631
- Chang, L. C., Chiu, P. Y., Salinas, C. C. J. H., Chen, S. P., Duann, Y., Liu, J. Y., et al. (2018). On the relationship between E region scintillation and ENSO observed by FORMOSAT-3/COSMIC. *J. Geophys. Res. Space Phys.* 123, 4053–4065. doi:10.1029/2018JA025299
- Chau, J. L., Goncharenko, L. P., Fejer, B. G., and Liu, H. L. (2012). Equatorial and low latitude ionospheric effects during sudden stratospheric warming events. *Space Sci. Rev.* 168, 385–417. doi:10.1007/s11214-011-9797-5
- Chum, J., Liu, J.-Y., Podolská, K., and Šindelářová, T. (2018). Infrasound in the ionosphere from earthquakes and typhoons. *J. Atmos. Sol. Terr. Phys.* 171, 72–82. doi:10.1016/j.jastp.2017.07.022
- Chum, J., and Podolská, K. (2018). 3D analysis of GW propagation in the ionosphere. *Geophys. Res. Lett.* 45(21), 11,562–11,571. doi:10.1029/2018GL079695
- Chum, J., Podolská, K., Ruzs, J., Baše, J., and Tedoradze, N. (2021). Statistical investigation of gravity wave characteristics in the ionosphere. *Earth Planets Space* 73, 60. doi:10.1186/s40623-021-01379-3
- Davies, K. (1990). *Ionospheric radio*. London: Peter Peregrinus Ltd. doi:10.1049/PBEW031E
- Dyson, P. L., Johnston, D. L., and Scali, J. L. (1995). Observations of gravity waves associated with mid-latitude spread-F. *Adv. Space Res.* 16, 113–116. doi:10.1016/0273-1177(95)00179-1
- Forbes, J. M., Palo, S. E., and Zhang, X. (2000). Variability of the ionosphere. *J. Atmos. Sol. Terr. Phys.* 62 (8), 685–693. doi:10.1016/S1364-6826(00)00029-8
- Fritts, D. C., and Alexander, M. J. (2003). Gravity wave dynamics and effects in the middle atmosphere. *Rev. Geophys.* 41 (1), 1003. doi:10.1029/2001RG000106
- Fritts, D. C., and Vadas, S. (2008). Gravity wave penetration into the thermosphere: Sensitivity to solar cycle variations and mean winds. *Ann. Geophys.* 26, 3841–3861. doi:10.5194/angeo-26-3841-2008
- Fritts, D. C., Vadas, S. L., Wan, K., and Werne, J. A. (2006). Mean and variable forcing of the middle atmosphere by gravity waves. *J. Atmos. Sol. Terr. Phys.* 68, 247–265. doi:10.1016/j.jastp.2005.04.010
- Goncharenko, L. P., Coster, A. J., Zhang, S. R., Erickson, P. J., Benkovich, L., Aponte, N., et al. (2018). Deep ionospheric hole created by sudden stratospheric warming in the nighttime ionosphere. *J. Geophys. Res. Space Phys.* 123, 7621–7633. doi:10.1029/2018JA025541
- Goncharenko, L., and Zhang, S.-R. (2008). Ionospheric signatures of sudden stratospheric warming: Ion temperature at middle latitude. *Geophys. Res. Lett.* 35, L21103. doi:10.1029/2008GL035684
- Guha, A., Paul, B., Chakraborty, M., and De, B. K. (2016). Tropical cyclone effects on the equatorial ionosphere: First result from the Indian sector. *J. Geophys. Res. Space Phys.* 121, 5764–5777. doi:10.1002/2016JA022363
- Hannawald, P., Schmidt, C., Sedlak, R., Wüst, S., and Bittner, M. (2019). Seasonal and intra-diurnal variability of small-scale gravity waves in OH airglow at two Alpine stations. *Atmos. Meas. Tech.* 12, 457–469. doi:10.5194/amt-12-457-2019
- Hannawald, P., Schmidt, C., Wüst, S., and Bittner, M. (2016). A fast SWIR imager for observations of transient features in OH airglow. *Atmos. Meas. Tech.* 9, 1461–1472. doi:10.5194/amt-9-1461-2016
- Huang, Ch.-S., Miller, C. A., and Kelley, M. C. (1994). Basic properties and gravity wave initiation of the midlatitude F region instability. *Radio. Sci.* 29 (1), 395–405. doi:10.1029/93RS01669
- Hung, R. J., Phan, T., and Smith, R. E. (1979). Coupling of ionosphere and troposphere during the occurrence of isolated tornadoes on November 20, 1973. *J. Geophys. Res.* 84, 1261–1268. doi:10.1029/JA084iA04p01261
- Jiang, C., Yang, G., Liu, J., Yokoyama, T., Komolmis, T., Song, H., et al. (2016). Ionosonde observations of daytime spread F at low latitudes. *J. Geophys. Res. Space Phys.* 121, 12,093–12,103. doi:10.1002/2016JA023123
- Jonah, O. F., Coster, A., Zhang, S., Goncharenko, L., Erickson, P. J., de Paula, E. R., et al. (2018). TID observations and source analysis during the 2017 memorial day weekend geomagnetic storm over north America. *J. Geophys. Res. Space Phys.* 123, 8749–8765. doi:10.1029/2018JA025367
- Kašpar, M., Müller, M., Kakos, V., Řezáčová, D., and Sokol, Z. (2009). Severe storm in bavaria, the Czech republic and Poland on 12–13 July 1984: A statistic- and model-based analysis. *Atmos. Res.* 93, 99–110. doi:10.1016/j.atmosres.2008.10.004
- Kašpar, M. (2003). Objective frontal analysis techniques applied to the extreme/non-extreme precipitation events. *Stud. Geophys. Geod.* 47, 639–640. doi:10.1023/A:1024771820322
- Kazimirovsky, E. S., and Kokourov, V. D. (1991). The tropospheric and stratospheric effects in the ionosphere. *J. Geomag. Geoelectr.* 43, 551–562. doi:10.5636/jgg.43.Supplement1_551
- Korenkov, Y. N., Klimenko, V. V., Klimenko, M. V., Bessarab, F. S., Korenkova, N. A., Ratovsky, K. G., et al. (2012). The global thermospheric and ionospheric response to the 2008 minor sudden stratospheric warming event. *J. Geophys. Res.* 117, A10309. doi:10.1029/2012JA018018
- Kouba, D., and Chum, J. (2018). Ground-based measurements of ionospheric dynamics. *J. Space Weather Space Clim.* 8, A29. doi:10.1051/swsc/2018018
- Kouba, D., and Koucká Knížová, P. (2012). Analysis of digisonde drift measurements quality. *J. Atmos. Sol. Terr. Phys.* 90–91, 212–221. doi:10.1016/j.jastp.2012.05.006
- Kouba, D., and Koucká Knížová, P. (2011). “Influence of non-vertical echos to ionogram scaling,” in *WDS’11 proceedings of contributed papers: Part II - physics of plasmas and ionized media*. Editors J. Šafránková, and J. Pavlů (Prague: MATFYZPRESS), 67–72.
- Kouba, D., and Koucká Knížová, P. (2016). Ionospheric vertical drift response at a mid-latitude station. *Adv. Space Res.* 58, 108–116. doi:10.1016/j.asr.2016.04.018
- Koucká Knížová, P., Laštovička, J., Kouba, D., Mošna, Z., Podolská, K., Potužníková, K., et al. (2021). Ionosphere influenced from lower-lying atmospheric regions. *Front. Astro. Space Sci.* 8, 1–29. doi:10.3389/fspas.2021.651445
- Koucká Knížová, P., Podolská, K., Potužníková, K., Kouba, D., Mošna, Z., Boška, J., et al. (2020). Evidence of vertical coupling: Meteorological storm fabienne on 23 september 2018 and its related effects observed up to the ionosphere. *Ann. Geophys.* 38, 73–93. doi:10.5194/angeo-38-73-2020
- Kramer, R., Wüst, S., and Bittner, M. (2016). Investigation of gravity wave activity based on operational radiosonde data from 13 years (1997–2009): Climatology and possible induced variability. *J. Atmos. Sol. Terr. Phys.* 140, 23–33. doi:10.1016/j.jastp.2016.01.014
- Kramer, R., Wüst, S., Schmidt, C., and Bittner, M. (2015). Gravity wave characteristics in the middle atmosphere during the CESAR campaign at Palma de Mallorca in 2011/2012: Impact of extratropical cyclones and cold fronts. *J. Atmos. Sol. Terr. Phys.* 128, 8–23. doi:10.1016/j.jastp.2015.03.001
- Laštovička, J., and Chum, J. (2017). A review of results of the international ionospheric Doppler sounder network. *Adv. Space Res.* 60 (8), 1629–1643. doi:10.1016/j.asr.2017.01.032
- Laštovička, J. (2006). Forcing of the ionosphere by waves from below. *J. Atmos. Sol. Terr. Phys.* 68, 479–497. doi:10.1016/j.jastp.2005.01.018
- Lay, E. H. (2018). Ionospheric irregularities and acoustic/gravity wave activity above low-latitude thunderstorms. *Geophys. Res. Lett.* 45, 90–97. doi:10.1002/2017GL076058
- Lǐ, W., Yue, J., Yang, Y., Li, Z., Guo, J., Pan, Y., et al. (2017). Analysis of ionospheric disturbances associated with powerful cyclones in East Asia and North America. *J. Atmos. Sol-Terr. Phys.* 161, 43–54. doi:10.1016/j.jastp.2017.06.012
- Medvedev, A. S., and Gavrilov, N. M. (1995). The nonlinear mechanism of gravity wave generation by meteorological motions in the atmosphere. *J. Atmos. Sol. Terr. Phys.* 57 (11), 1221–1231. doi:10.1016/0021-9169(95)00008-p
- Mitchell, N. J., and Howells, V. St. C. (1998). Vertical velocities associated with gravity waves measured in the mesosphere and lower thermosphere with the ELSCAT VHF radar. *Ann. Geophys.* 16, 1367–1379. doi:10.1007/s00585-998-1367-0
- Mošna, Z., Edemskiy, I., Laštovička, J., Kozubek, M., Koucká Knížová, P., Kouba, D., et al. (2021). Observation of the ionosphere in middle latitudes during 2009, 2018 and 2018/2019 sudden stratospheric warming events. *Atmosphere* 12 (5), 602. doi:10.3390/atmos12050602

- Nicolls, M. J., and Kelley, M. C. (2005). Strong evidence for gravity wave seeding of an ionospheric plasma instability. *Geophys. Res. Lett.* 32, L05108. doi:10.1029/2004GL020737
- Pancheva, D., Mukhtarov, P., Mitchell, N. J., Merzlyakov, E., Smith, A. K., Andonov, B., et al. (2008). Planetary waves in coupling the stratosphere and mesosphere during the major stratospheric warming in 2003/2004. *J. Geophys. Res.* 113, D12105. doi:10.1029/2007JD009011
- Pavelin, E., and Whiteway, J. A. (2002). Gravity wave interactions around the jet stream. *Geophys. Res. Lett.* 29 (21), 21–24. doi:10.1029/2002GL015783
- Pedatella, N. M., and Forbes, J. M. (2010). Evidence for stratosphere sudden warming-ionosphere coupling due to vertically propagating tides. *Geophys. Res. Lett.* 37, L11104. doi:10.1029/2010GL043560
- Pedatella, N. M., and Liu, H.-L. (2018). The influence of internal atmospheric variability on the ionosphere response to a geomagnetic storm. *Geophys. Res. Lett.* 45, 4578–4585. doi:10.1029/2018GL077867
- Pezzopane, M., Fagundes, P. R., Ciruolo, L., Correia, E., Cabrera, M. A., and Ezquer, R. G. (2011). Unusual nighttime impulsive foF2 enhancement below the southern anomaly crest under geomagnetically quiet conditions. *J. Geophys. Res. Space Phys.* 116, A12314. doi:10.1029/2011JA016593
- Pierce, A. D., and Coroniti, S. C. (1966). A mechanism for the generation of acoustic-gravity waves during thunderstorm formation. *Nature* 210, 1209–1210. doi:10.1038/2101209a0
- Pröls, G. W. (1995). “Ionospheric F-region storms,” in *Handbook of atmospheric electrodynamics*. Editor H. Volland (Boca Raton, FL: CRC Press), Vol. II, 195–248.
- Radicella, S. M., and Migoya-Orué, Y. O. (2021). “GNSS-derived data for the study of the ionosphere,” in *GPS and GNSS technology in Geosciences*. Editors G. Petropoulos, and P. Srivastava (Elsevier), 221–239.
- Rahmani, Y., Alizadeh, M. M., Schuh, H., Wickert, J., and Tsai, L. C. (2020). Probing vertical coupling effects of thunderstorms on lower ionosphere using GNSS data. *Adv. Space Res.* 66 (8), 1967–1976. doi:10.1016/j.asr.2020.07.018
- Rishbeth, H., and Mendillo, M. (2001). Patterns of F2-layer variability. *J. Atmos. Sol. Terr. Phys.* 63, 1661–1680. doi:10.1016/S1364-6826(01)00036-0
- Šauli, P., and Boška, J. (2001). Tropospheric events and possible related gravity wave activity effects on the ionosphere. *J. Atm. Sol. Terr. Phys.* 63, 945–950. doi:10.1016/S1364-6826(00)00205-4
- Siddiqui, T. A., Yamazaki, Y., Stolle, C., Maute, A., Laštovička, J., Edemskiy, I. K., et al. (2021). Understanding the total electron content variability over Europe during 2009 and 2019 SSWs. *J. Geophys. Res. Space Phys.* 126, e2020JA028751. doi:10.1029/2020JA028751
- Smith, A. (1996). Longitudinal variations in mesospheric winds: Evidence for gravity wave filtering by planetary waves. *J. Atmos. Sci.* 53 (8), 1156–1173. doi:10.1175/1520-0469(1996)053<1156:lvimwe>2.0.co;2
- Taylor, M. J., and Hapgood, M. A. (1988). Identification of a thunderstorm as a source of short period gravity waves in the upper atmospheric nightglow emissions. *Planet. Space Sci.* 36 (10), 975–985. doi:10.1016/0032-0633(88)90035-9
- Vadas, S. L., Makela, J. J., Nicolls, M. J., and Milliff, R. F. (2015). Excitation of gravity waves by ocean surface wave packets: Upward propagation and reconstruction of the thermospheric gravity wave field. *J. Geophys. Res. Space Phys.* 120 (11), 9748–9780. doi:10.1002/2015JA021430
- Wakai, N., Ohya, H., and Koizumi, T. (1987). “Ministry of posts and telecommunications,” in *Manual of ionogram scaling* (Tokyo: Radio Research Laboratory), 3rd Version.
- Wüst, S., Bittner, M., Espy, P. J., French, W. J. R., and Mulligan, F. J. (2023). Hydroxyl airglow observations for investigating atmospheric dynamics: Results and challenges. *Atmos. Chem. Phys.* 23, 1599–1618. doi:10.5194/acp-23-1599-2023
- Wüst, S., Bittner, M., Yee, J.-H., Mlynczak, M. G., and Russell, J. M. (2017). Variability of the Brunt–Väisälä frequency at the OH* layer height. *Atmos. Meas. Tech.* 10, 4895–4903. doi:10.5194/amt-10-4895-2017
- Xiao, S. G., Xiao, Z., Shi, J. K., Zhang, D. H., Feng, X. S., Hao, Y. Q., et al. (2009). Observational facts in revealing a close relation between acoustic-gravity waves and midlatitude spread F. *J. Geophys. Res. Space Phys.* 114, A01303. doi:10.1029/2008JA013747
- Xiao, S., Shi, J., Zhang, D., Hao, Y., and Huang, W. (2012). Observational study of daytime ionospheric irregularities associated with typhoon. *Sci. China Technol. Sci.* 55, 1302–1304. doi:10.1007/s11431-012-4816-7
- Xiao, Z., Xiao, S., Hao, Y., and Zhang, D. (2007). Morphological features of ionospheric response to typhoon. *J. Geophys. Res.* 112, A04304. doi:10.1029/2006JA011671
- Yigit, E., and Medvedev, A. S. (2015). Internal wave coupling processes in Earth’s atmosphere. *Adv. Space Res.* 55 (4), 983–1003. doi:10.1016/j.asr.2014.11.020
- Yu, S., Xiao, Z., Aa, E., Hao, Y., and Zhang, D. (2016). Observational investigation of the possible correlation between medium-scale TIDs and mid-latitude spread F. *Adv. Space Res.* 58, 349–357. doi:10.1016/j.asr.2016.05.002
- Yue, J., Miller, S. D., Hoffmann, L., and Straka III, W. C. (2014). Stratospheric and mesospheric concentric gravity waves over tropical cyclone Mahasen: Joint AIRS and VIIRS satellite observations. *J. Atmos. Sol-Terr. Phys.* 119, 83–90. doi:10.1016/j.jastp.2014.07.003
- Zakharov, V. I., and Sigachev, P. K. (2022). Ionospheric disturbances from tropical cyclones. *Adv. Space Res.* 69 (1), 132–141. doi:10.1016/j.asr.2021.09.025